Ocean Modelling 25 (2008) 17–34

Contents lists available at ScienceDirect

Ocean Modelling

journal homepage: www.elsevier.com/locate/ocemod

Inverse barotropic tidal estimation for regional ocean applications

O.G. Logutov *, P.F.J. Lermusiaux

Massachusetts Institute of Technology, Department of Mechanical Engineering, 77 Massachusetts Avenue, Room 5-207B, Cambridge, MA 02139, USA

ARTICLE INFO

Article history:
Received 29 January 2008
Received in revised form 21 May 2008
Accepted 11 June 2008
Available online 25 June 2008

ABSTRACT

Correct representation of tidal processes in regional ocean models is contingent on the accurate specification of open boundary conditions. This paper describes a new inverse scheme for the assimilation of observational data into a depth-integrated spectral shallow water tidal model and the numerical implementation of this scheme into a stand-alone computational system for regional tidal prediction. A novel aspect is a specific implementation of the inverse which does not require an adjoint model. An optimization is carried out in the open boundary condition space rather than in the observational space or model state space. Our approach reflects the specifics of regional tidal modeling applications in which open boundary conditions (OBCs) typically constitute a significant source of uncertainty. Regional tidal models rely predominantly on global tidal estimates for open boundary conditions. As the resolution of global tidal models is insufficient to fully resolve regional topographic and coastal features, the a priori OBC estimates potentially contain an error. It is, therefore, desirable to correct these OBCs by finding an inverse OBC estimate that is fitted to the regional observations, in accord with the regional dynamics and respective error estimates. The data assimilation strategy presented in this paper provides a consistent and practical estimation scheme for littoral ocean science and applications where tidal effects are significant. Illustrations of our methodological and computational results are presented in the area of Dabob Bay and Hood Canal, WA, which is a region connected to the open Pacific ocean through a series of inland waterways and complex shorelines and bathymetry.

1. Introduction

Coastal dynamical phenomena can be significantly affected by tidal processes. Tidal currents constitute a dominant component of circulation in many coastal areas, with velocities of 50–150 cm/s being common (e.g., Moody et al., 1984). Tidally driven currents may generate complex cross-shelf particle transports, highly horizontally inhomogeneous barotropic flow patterns, as well as important secondary tidally-driven features, such as internal tides, internal waves, tidal mixing and tidal fronts (Chen and Beardsley, 1998). Tidal processes are also important for ocean ecosystem dynamics on a regional scale. For example, distinct patterns of nutrient patchiness, have been observed in some tidally active basins; arguably controlled by tidal processes (e.g., Franks and Chen, 1996). Correct representation of these tidal processes in regional ocean models is paramount but challenging.

Accurate barotropic tidal estimates (tidal elevations, transports, and velocities) are needed in numerous oceanographic applications. These include physical modeling and acoustical, chemical, biological, and eco-system modeling applications. For example, the determination of the internal tides requires an accurate knowledge of barotropic transports and flows across bottom topography as such flows are utilized as forcing in internal tide models (Baines, 1982; Garrett and Gerkema, 2007). These internal tide models, in their turn, are needed in acoustical (Lermusiaux and Chiu, 2002) and biological applications (e.g., Besiktepe et al., 2003) because the vertical velocity field and the temperature and density perturbations induced by internal tides and wave are consequential in these applications. The "state-of-the-art" for modeling tidal phenomena in regional ocean applications is currently based on forcing primitive equation (PE) or non-hydrostatic ocean models with barotropic tidal fields. This tidal forcing is applied through open boundary and initial flow conditions. If the horizontal and vertical model resolutions are sufficient and accurate regional barotropic tidal forcing is used, this approach can simulate a large spectrum of tidally driven processes. For example, effects of internal tides and waves can be generated and represented statistically and possibly deterministically in limited regions.

Regional tidal models rely on global tidal models (Shum et al., 1997), larger scale models, and/or extrapolation from local tide gauges for open boundary conditions (OBCs). For example, the two Navy tidal modeling systems, ADCIRC (Luettich et al., 1992) and PCtides (Hubbert et al., 2001), use the tidal harmonic constituents extracted from the global FES95 solutions (LeProvost et al., 1994), as well as extrapolation from local tide gauges (Blain et al., 2002). Greenberg et al. (2005) obtain the OBCs for the Quoddy region of the Bay of Fundy from an outer Bay of Fundy regional

* Corresponding author. Tel.: +1 617 324 3541; fax: +1 617 324 3541.
E-mail addresses: logutov@mit.edu (O.G. Logutov), pierrel@mit.edu (P.F.J. Lermusiaux).

1463-5003/$ - see front matter © 2008 Elsevier Ltd. All rights reserved.
doi:10.1016/j.ocemod.2008.06.004

model. Foreman and Thomson (1997) use the elevation amplitudes and phases at the southern and western boundaries around the coast of Vancouver Island from a combination of offshore pressure tide gauges and the global tidal model of Egbert et al. (1994). Correct representation of tidal processes on a regional scale is contingent on the accurate specification of OBCs. Errors in OBCs can generate physically unrealistic flow fields and lead to large interior data-model misfits. It is, therefore, desirable to tune the OBCs to local observations.

The need for dynamical constraints to optimally extrapolate reliable sea level data on the coastline to tidal model open boundaries has long been recognized (Bennett and McIntosh, 1982). A variety of methods have been developed to constrain regional barotropic tidal estimates using tidal elevation and velocity observations (see Section 2). Despite of wide recognition that a quantitative fit of the OBCs to local observational data is highly desirable, it is often omitted or carried out by simple trial and error through the comparison of model outputs with tidal elevation amplitudes and phases at local tide gauge stations (e.g., Foreman and Thomson, 1997; Greenberg et al., 2005) among others. This implicitly attests to the fact that new methods to fit OBCs to data, that are practical and amenable to quick implementation, are still needed. The data assimilation strategy presented in this paper is designed specifically to provide a highly practical and quantitative technique for the fit of OBCs to tidal data in regional tidal modeling applications.

This paper describes new forward and inverse schemes for estimating regional barotropic tidal flows and the numerical implementation of these schemes into a stand-alone computational system. The data-driven prognostic schemes are based on solving the depth-integrated shallow water equations as a boundary value problem in the spectral domain. With our system, regional barotropic tides can be computed at very high resolution in multiple nested domains. The observational data are assimilated into the tidal model through a practical inverse method. The outputs of the system are accurate high-resolution barotropic tidal fields that can be utilized to force the open boundary of any modern regional PE or non-hydrostatic ocean model. Synthesis of observations and numerical models has long been recognized as a necessary step towards successful coastal prediction (Robinson et al., 1998; Lermusiaux, 2006). With our new procedures, the measurements are assimilated in such a way that the inverse tidal estimates satisfy the shallow water equations exactly.

Our barotropic tidal estimation system can be used for specific tidal studies and for forcing PE and internal wave models. Presently, it is illustrated with the Harvard Ocean Prediction System (HOPS), an interdisciplinary primitive equation modeling system designed primarily for regional ocean applications with advanced data assimilation (DA) (Robinson, 1999; Lermusiaux, 1999). The free-surface version of HOPS requires barotropic tidal forcings (tidal sea surface height and barotropic velocity components) at open boundaries and for initialization. These barotropic tidal forcings are obtained using the new forward–inverse system described in this paper. Because the barotropic tidal model is designed to simulate a specific process and serve a specific range of spatial-temporal scales, we are able to simulate the barotropic tides at very high resolution and tune its OBCs and model parameters to available regional tide gauges and Acoustic Doppler Current Profiler (ADCP) data. This new methodology is an example of a multi-model approach, with several specialized models combined together in a single ocean prediction system. More general discussion of uncertainties and implementation of multi-model simulations are provided in Logutov and Robinson (2005), Logutov (2007), Evangelinos et al. (2006), Lermusiaux et al., 2004.

We have exercised our tidal modeling approach in multiple regional applications. These include real-time modeling in the Middle Atlantic Bight and the shelf-break front region off the coast of New Jersey, as part of the Autonomous Wide Aperture Cluster for Surveillance (AWACS-06) and Shallow Water (SW06) experiments, in the California Current System and Monterey Bay region as part of the Monterey Bay-06 (MB06) experiment which followed our work during AOSN-II (Haley et al., in press; Lermusiaux, 2007) in that region, and in the Hood Canal and Dabob Bay region, WA, as part of the PLUSNet-07 (PN07) experiment (Xu et al., 2008). Our tidal modeling work in the Hood Canal and Dabob Bay, particularly challenging given the complexity of shoreline and bottom topography of the inland waterways connecting this basin to the ocean, is selected here to exemplify our approach and method.

The paper is organized as follows. Existing regional tidal models and assimilation schemes pertinent to the new techniques described in this paper are briefly reviewed next (Section 2). In Section 3, the dynamical equations for linearized barotropic shallow water dynamics and the corresponding boundary value problem in the spectral domain are outlined. Section 4 covers the numerical solution of the dynamical equations, with details of the numerical implementation provided in Appendix B. Section 5 describes the proposed method of inverse estimation of OBCs designed for regional tidal modeling. Discussion of our method and its comparison to the *representer* method, an approach for DA utilized in global tidal modeling (Egbert et al., 1994; Egbert and Erofeeva, 2002), are given in Section 6. Finally, Section 7 presents an illustration of a real-world tidal modeling application within the framework of the Persistent Littoral Undersea Surveillance Network (PLUSNet) project in the Dabob Bay/Hood Canal region of WA. Appendices A through D detail the notation, the specifics of our numerical implementation, and of the conversion of data from time to model spectral domain and back, respectively.

2. A synopsis of tidal modeling and data assimilation

A variety of methods for barotropic tidal modeling has been developed and analyzed in the literature. Differences among these methods are in the formulation of the horizontal coordinates, in the inclusion or omission of the vertical structure of tidal velocity fields, and in the treatment of the time dependency and of the non-linear terms. The horizontal coordinate formulations include finite-difference schemes (e.g., Davies, 1993; Hubbert et al., 2001), finite-element schemes (e.g., LeProvost and Vincent, 1986; Luettich et al., 1992; Greenberg et al., 2005; Bernard et al., 2008), and structured non-orthogonal curvilinear coordinate schemes (e.g., George, 2007). Two-dimensional (e.g., McLaughlin et al., 2003) and three-dimensional (e.g., Jones and Davies, 1996; Davies et al., 1997c) barotropic tidal models have been proposed to allow for omission or inclusion of the computation of bottom and surface boundary layers as well as of the vertical current structure, especially effects of turbulent fluxes and their parameterizations (e.g., Davies, 1993; Davies and Gerritsen, 1994; Davies et al., 1997b; Foreman and Thomson, 1997; Lee and Jung, 1999). The models differ by their treatment of the time dependency and fall into classes of time-domain (e.g., Le Cann, 1990; Lynch and Gray, 1979) and spectral-domain (e.g., LeProvost et al., 1981; Lynch and Naimie, 1993; Davies et al., 1997a) models.

Two alternative treatments of the time dependency, by time stepping (e.g., Lynch and Gray, 1979) and by spectral representation (e.g., LeProvost et al., 1981), have been exercised. The spectral domain representation assumes harmonic time dependency for each tidal constituent and leads to a substantial reduction of model computational complexity and, therefore, potentially to higher resolution models. The coupling between different tidal frequencies that arises from the nonlinear interactions can be included in the spectral domain models using a perturbation method (Snyder et

al., 1979). A review of spectral domain tidal models in regional ocean applications is provided by Davies et al. (1997a). In addition to substantial computational efficiency, spectral domain models are easier in use and, as such, more suitable for dissemination among a wider audience of researchers. The time stepping models, on the other hand, are more amenable to inclusion of the nonlinear terms and more suitable for modeling ocean response to a general time-dependent meteorological forcing (e.g., Luettich et al., 1992).

The relative importance of the various nonlinear mechanisms for regional barotropic tidal modeling is reviewed by Parker (1991). Theoretically, nonlinear processes act as an agent for energy transfer to higher harmonics and are capable of introducing new frequencies in tidal spectrum. A number of fully nonlinear regional tidal models have been developed (Le Cann, 1990, among others; Luettich et al., 1992; George, 2007). The nonlinear tidal effects can also be simulated by using the primitive equation or non-hydrostatic models with the open boundary tidal forcing prescribed from the tidal models. If open ocean boundaries of a PE model are selected away from the shallow-water regions, significant gains in accuracy can result from using linearized high-resolution data-assimilative barotropic tidal models, rather than their non-linear counterparts, to prescribe the tidal open boundary forcing for PE models.

A number of methods have been developed to include the nonlinear tidal effects within the linearized modeling framework. For example, the *shallow-water* tidal constituents can be introduced to compensate for kinematic and dissipative nonlinearities and for wave–wave interactions between the astronomical constituents (LeProvost et al., 1981; Andersen et al., 2006). The characteristics of the shallow-water constituents can either be empirically determined from the observational data (e.g., Hea et al., 2004; Simpson, 1998) or obtained analytically using a classical perturbation method (LeProvost et al., 1981). In the latter case, the fully nonlinear problem can be reduced to a sequence of linearized boundary value problems, similar to the boundary value problem described in Section 3, for each successive order of approximation of the perturbation method (e.g., LeProvost and Vincent, 1986). In practice, the perturbation sequence is typically limited to the second order. These developments provide a rigorous framework for full inclusion of the nonlinear effects into robust high-resolution linearized data-assimilative computations.

Importantly, all regional tidal modeling systems require specification of the open boundary conditions (OBCs). The early coastal tidal DA and parameter estimation work is reviewed in Sections 5.1–2 of Robinson et al. (1998). Bennett and McIntosh (1982) developed a variational formulation to consistently constrain regional tidal estimates with local observations. The formulation is in the time domain. It solves the equations of the first variation of the quadratic cost function penalizing model-data misfits as well as deviations of the generalized inverse solution from the forward model solution, weighted by observational and model error covariance estimates. This generalized inverse methodology was further applied for modeling M2 tides in Bass Strait north of Tasmania (McIntosh and Bennett, 1984) and has become a foundation for a variety of representer methods for tidal data inversion, interpolation, and inference (Egbert, 1997). For instance, Egbert et al. (1994) assimilate TOPEX/POSEIDON altimeter data and tide gauge data into global barotropic tidal models. The method requires formulation of an adjoint tidal model. An optimization is carried out in the observational space by generalized inversion (Bennett, 1992; Bennett, 2002). Reduced-basis alternatives of the representer method have latter been applied for tidal DA (Egbert and Erofeeva, 2002). Representer-based inverse models have also been formulated for estimation of the internal tides (Kurapov et al., 2003), as well as other coastal ocean modeling problems (Kurapov et al., 2007). Hybrid schemes have also been developed. For example, He and Wilkin (2006) have successfully utilized a full primitive equation model with uniform density to obtain the nonlinear forward tidal solution. Subsequently, a linear, frequency-domain, finite-element model is employed for the inverse problem, assimilating tidal observations by minimizing a least-square data-model misfit criterion. Zou et al. (1995) also developed a sequential open-boundary control scheme augmenting radiation conditions and applied it to idealized barotropic wind-driven ocean simulations.

Kalman Filtering (KF) and other sequential DA techniques have been extensively applied in the context of deterministic and stochastic hydrodynamic, water quality, and surface wave regional forecasting and hind-casting and for error covariance modeling (e.g., see Section 5 in Robinson et al., 1998). For example, the KF approach has recently been adopted as an operational method for assimilation of sea-level measurements into the Dutch Continental Shelf model utilized at the Dutch Meteorological Institute to predict water levels along the Dutch coast and the three-dimensional flow fields in the North and the Baltic sea basins (Sorensen and Madsen, 2004). Other examples include operational shelf sea modeling in Danish waters carried out at the Danish Meteorological Institute (Canizares et al., 2001). Kalman filter algorithms rely on propagating an uncertainty in the model state-space using linearized error covariance evolution equations or Monte–Carlo techniques. The error covariance evolution is formulated in the state-space form, with gridded water levels, velocities, and the uncertain parameters included in a state vector. Low-rank and ensemble approximations have been described and applied in realistic settings, and various regularization techniques for error covariance and Kalman gain estimation have been introduced, including temporal smoothing, the steady-state approximation, and spatial regularization, among others (Sorensen and Madsen, 2004). An efficient KF data assimilation procedure for weakly nonlinear regional tidal models has been formulated by Heemink and Kloosterhuis (1990). The dynamical equations were embedded into a stochastic environment and the state-space was evolved using the non-linear stochastic shallow water equations to obtain a constant-gain extended-KF approximation. The steady-state KF method is founded on an observation that error covariances often tend to a quasi-steady state after a few days of assimilation. Therefore, a time invariant Kalman gain could be obtained off-line and applied without the need to be recomputed as new measurements became available. The method was originally applied for assimilation of water level measurements into a tidal model of the North Sea and, subsequently, in numerous other applications in simulated and realistic settings (Canizares et al., 2001; Sorensen and Madsen, 2004). A main difficulty of the KF-based algorithms is related to the quantification of the stochastic noise processes or model error covariance parameters employed in the scheme (Dee, 1995; Lermusiaux, 2006; Lermusiaux et al., 2006). Other DA practices in regional tidal modeling include use of weighted nudging to loosely constrain model tidal heights to observed sea-level elevations at available tidal stations (e.g., Navy PCTides system of Hubbert et al., 2001). Das and Lardner (1992) use water depth and bottom friction coefficients as tunable parameters in a depth-averaged linearized tidal model in the time domain. They employ an adjoint scheme to solve the optimization problem of fitting the tunable parameters to observations.

The new regional DA scheme developed in this paper differs from the previous schemes mostly in two ways. Firstly, an optimization is carried out in the open boundary condition space rather than in the observational space or full state space. Our strategy of using the OBCs as the control space for data assimilation reflects the specifics of regional tidal modeling. Secondly, our approach does not require an adjoint model. The specifics of the implementation are such that only the forward dynamical model is needed.

Of course, variations of our approach and hybrid schemes are possible. They are outlined in the conclusions.

3. Dynamical equations

Regional and global tidal flow fields are predominantly controlled by different types of tide-generating forcing. In global tidal models, the forcing is provided by direct astronomical gravitational forces prescribed through a tide-generating potential. In regional applications, tidal forcing is primarily provided through the open boundary conditions. In shallow water, direct astronomical forcing is negligible as compared to open boundary forcing and can be omitted from the hydrodynamic equations (Snyder et al., 1979; Simpson, 1998). Similarly, tidal loading effects related to the deformation of the earth crust under the load of a tidal wave, important for global tidal modeling, are negligible in regional applications. In the present paper, we are concerned exclusively with shallow sea regions and, therefore, the tide generating forces and tidal loading corrections can be omitted from the hydrodynamic equations.

3.1. Time domain

Given a regional basin Ω, with open boundary segments $\partial\Omega_O$ and closed boundary segments $\partial\Omega_C$, the linearized barotropic shallow water equations are derived from vertical integration over the water column of the three-dimensional momentum and continuity equations subject to the hydrostatic and Boussinesq approximations (Lynch and Gray, 1979). Using spherical coordinates in the horizontal, we obtain

$$\begin{aligned}
&\frac{\partial}{\partial t}\eta + \frac{1}{a\cos\phi}\frac{\partial}{\partial\lambda}(Hu) + \frac{1}{a\cos\phi}\frac{\partial}{\partial\phi}(Hv\cos\phi) = 0\\
&\frac{\partial}{\partial t}u - fv + F_\lambda = \frac{-g}{a\cos\phi}\frac{\partial}{\partial\lambda}\eta\\
&\frac{\partial}{\partial t}v + fu + F_\phi = \frac{-g}{a}\frac{\partial}{\partial\phi}\eta
\end{aligned} \tag{1}$$

for $(\lambda,\phi)\in\Omega$, subject to open boundary conditions

$$\eta|_{\partial\Omega_O} = \eta_{obc} \tag{2}$$

and closed boundary conditions

$$\mathbf{n}\cdot\mathbf{u}|_{\partial\Omega_C} = 0. \tag{3}$$

In the foregoing, η and $\mathbf{u} = (u, v)$ denote tidal elevation and zonal and meridional velocity components, λ, ϕ, and a are the longitude, latitude, and earth radius, H, g, and f denote the undisturbed water depth, acceleration due to gravity, and the Coriolis parameter, and F_λ and F_ϕ are the parameterized friction forces in the zonal and the meridional directions, respectively. Inherent in Eq. (1) is omission of the non-linear advective terms $(\mathbf{u}\cdot\nabla)\mathbf{u}$. We will further require that the dissipative terms F_λ and F_ϕ are also linearized in some fashion. The linearization is introduced in order to make the governing equations amenable to reduction to a linear system of algebraic equations once they are discretized on a selected grid. As mentioned in Section 1, linearized models have an important role and multiple applications. Quadratic friction of the form

$$F_\lambda = C_D|\mathbf{u}|u/H, \qquad F_\phi = C_D|\mathbf{u}|v/H \tag{4}$$

with non-dimensional bottom drag coefficient $C_D = 0.002 - 0.003$ is typically suggested for depth-averaged barotropic tidal models (Grenier et al., 1995). Linearization of quadratic dissipation terms $F_\lambda \approx \kappa(\lambda,\phi)u, F_\phi \approx \kappa(\lambda,\phi)v$, with a spatially varying damping coefficient $\kappa(\lambda,\phi)$, can be obtained for example using the perturbation method developed by LeProvost et al. (1981). Alternatively, an iterative approach can be applied in which the 0th iteration of the solution is obtained with a constant value of κ, while the next iteration solution utilizes the barotropic velocities obtained in the previous iteration for $|\mathbf{u}|$ in (4). We follow the latter approach, with one iteration. A detailed review of bottom friction parameterizations suitable for barotropic ocean tidal models is beyond the scope of this paper but has been addressed in a number of papers (Grenier et al., 1995; Xing and Davies, 1996; Davies et al., 1997b; Lee and Jung, 1999). With Eq. (1), the linearized barotropic tidal estimates can be obtained and tuned to local observations of barotropic tides. Nonlinear tidal effects can then be simulated, if needed, by the PE models forced by these linearized barotropic tides at open-boundaries. Such approach is acceptable if tidal velocities are small enough at the offshore open-boundary of a PE model. With these considerations in mind, our focus here is the linearized inverse barotropic tidal estimation and data assimilation in regional applications.

System (1) is forced through open boundary conditions η_{obc}. In regional applications, the open boundary conditions are often specified from global tidal models (Shum et al., 1997). Global tidal models typically compute estimates for individual astronomical tidal constituents. Astronomical tidal constituent frequencies correspond to combinations of fundamental astronomical frequencies arising from planetary motions (e.g., Simpson, 1998). Each astronomical constituent is defined by a unique set of Doodson numbers which determine its frequency. We specify the open boundary condition (2) from a global tidal model as a superposition of K tidal constituents estimated to be significant for the given coastal region of interest:

$$\eta_{obc} = \mathbb{R}\left\{\sum_{k=1}^{K}\zeta_k(x_O,y_O)\exp\ \mathrm{i}\omega_k t\right\}, \tag{5}$$

where $\mathbb{R}$ denotes the real parts. Complex $\zeta_k(x_O,y_O)$ specifies spatial variations of boundary forcing in amplitude and phase for the kth tidal constituent along open boundary segments, $(x_O,y_O)\in\partial\Omega_O$. In our own practice, we utilize global tidal fields of TPXO 7.0 from OSU (Egbert et al., 1994) for $\zeta_k(x_O,y_O)$ in forward computations in the outer domain and the outer domain solution in the nested domains. We select the K significant tidal constituents in Eq. (5) by analysis of tidal gauges and other current data in the given coastal region of interest.

Several OBCs other than (5) can be implemented with our scheme, as discussed in Tsynkov (1998), Marchesiello et al. (2001), Oddo and Pinardi (2008), Blayo and Debreu (2005). They include radiation-based and characteristic boundary conditions (e.g., Orlanski, 1976; Flather, 1976; Chapman, 1985; Shulman et al., 2002) as well as relaxation conditions and absorbing (sponge) layers (e.g., Davies, 1976; Marchesiello et al., 2001; Lavelle and Thacker, 2008). These OBCs for the barotropic tidal model should be consistent with the OBCs used in the primitive equation model (forced by tides) and should account for the different scales and resolutions. The OBCs used in HOPS, including radiation, relaxation, simplified physics and advection-based conditions are reviewed in Lermusiaux (1997).

In anticipation of reduction of the governing equations to a linear system of algebraic equations for the discretized model state-space, we introduce the matrix notation and express (1) as

$$\frac{\partial}{\partial t}\eta + \nabla\cdot\begin{bmatrix}Hu\\ Hv\end{bmatrix} = 0 \tag{6}$$

$$\begin{bmatrix}\frac{\partial}{\partial t}+\kappa & -f\\ f & \frac{\partial}{\partial t}+\kappa\end{bmatrix}\begin{bmatrix}u\\ v\end{bmatrix} = -g\nabla\eta \tag{7}$$

where $\nabla\cdot$ and ∇ are the divergence and gradient operators in spherical coordinates. Eqs. (6) and (7) are solved in the spectral domain in terms of the prognostic variable η. The velocity field is subsequently obtained from η via (7). The details of the solution now follow.

3.2. Spectral domain

The forced response of a linear dynamical system (6) and (7) contains K tidal constituent frequencies provided in the open boundary conditions (5). The solution can be obtained in the form

$$\{\eta,u,v\}(\lambda,\phi,t)=\mathbb{R}\left\{\sum_{k=1}^{K}\{\tilde{\eta}_k,\tilde{u}_k,\tilde{v}_k\}(\lambda,\phi)\exp \mathrm{i}\omega_k t\right\} \tag{8}$$

By substituting (8) into (6) and (7), we obtain for each individual tidal constituent k

$$\mathrm{i}\omega_k\ \tilde{\eta}_k+\nabla\cdot\begin{bmatrix}H\tilde{u}_k\\ H\tilde{v}_k\end{bmatrix}=0 \tag{9}$$

$$\begin{bmatrix}\mathrm{i}\omega_k+\kappa & -f\\ f & \mathrm{i}\omega_k+\kappa\end{bmatrix}\begin{bmatrix}\tilde{u}_k\\ \tilde{v}_k\end{bmatrix}=-g\nabla\tilde{\eta}_k \tag{10}$$

subject to boundary conditions

$$\tilde{\eta}_k|_{\partial\Omega_O}=\zeta_k(x_O,y_O) \tag{11}$$

at open boundaries, and

$$\mathbf{n}\cdot\begin{bmatrix}\tilde{u}_k\\ \tilde{v}_k\end{bmatrix}|_{\partial\Omega_C}=0 \tag{12}$$

at closed boundaries, with $\mathbf{n}=[n_x,n_y]^{\mathrm{T}}$ denoting a coastal boundary normal, as before. Eqs. (10)–(12) constitute an elliptic boundary value problem. Denote

$$\mathbf{F}\equiv\begin{bmatrix}\mathrm{i}\omega_k+\kappa & -f\\ f & \mathrm{i}\omega_k+\kappa\end{bmatrix} \tag{13}$$

The entries of the matrix $\mathbf{F}$ are spatially varying fields. The determinant of $\mathbf{F}$

$$|\mathbf{F}|=(\mathrm{i}\omega_k+\kappa)^2+f^2 \tag{14}$$

is non-zero given $\omega_k\neq f$ or $\kappa\neq 0$. If the tidal constituent frequency matches the local Coriolis frequency, $\omega_k=f$, a resonant condition occurs. The resonance is dampened through the dissipation terms and, therefore, the form of the dissipation parameterization is particularly important in the areas with $\omega_k\approx f$. With $\kappa\neq 0$, the inverse $\mathbf{F}^{-1}$ always exists given by

$$\mathbf{F}^{-1}=\frac{1}{(\mathrm{i}\omega_k+\kappa)^2+f^2}\begin{bmatrix}\mathrm{i}\omega_k+\kappa & f\\ -f & \mathrm{i}\omega_k+\kappa\end{bmatrix}. \tag{15}$$

The velocities $(\tilde{u}_k,\tilde{v}_k)$ are obtained from $\tilde{\eta}_k$ as

$$\begin{bmatrix}\tilde{u}_k\\ \tilde{v}_k\end{bmatrix}=\frac{-g}{(\mathrm{i}\omega_k+\kappa)^2+f^2}\begin{bmatrix}\mathrm{i}\omega_k+\kappa & f\\ -f & \mathrm{i}\omega_k+\kappa\end{bmatrix}\nabla\tilde{\eta}_k. \tag{16}$$

By substituting (16) into (9), we obtain an equation for a single prognostic variable

$$\mathscr{L}\{\tilde{\eta}_k\}=0 \tag{17}$$

with an elliptic second order linear operator $\mathscr{L}\{\cdot\}$

$$\mathscr{L}\{\cdot\}=\left(\mathrm{i}\omega_k\nabla\cdot\frac{gH}{(\mathrm{i}\omega_k+\kappa)^2+f^2}\begin{bmatrix}\mathrm{i}\omega_k+\kappa & f\\ -f & \mathrm{i}\omega_k+\kappa\end{bmatrix}\nabla\right). \tag{18}$$

Eq. (17) is solved with the boundary conditions (11) and (12). Our specific numerical implementation of the solution is discussed in the next section.

Conversion of data and the model outputs from the time domain to spectral domain and back is discussed in detail in Appendix D. Although this task might be considered as trivial, clarification of conventions and details presented in this appendix are helpful for practical purposes.

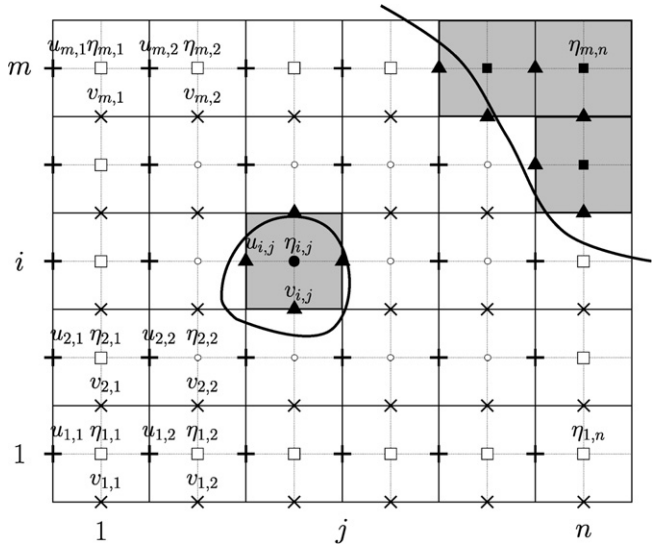

Fig. 1. Schematic of staggered Arakawa-C grid. Solid lines represent coastlines, filled symbols are masked nodes. Elevation η, zonal u and meridional v velocity nodes shown with "o", "+", and "x" symbols, respectively. Active, open boundary, and masked nodes depicted as unfilled circles, unfilled squares, and filled circles/squares, respectively.

4. Discrete model operators

Eq. (17) with the boundary conditions (11) and (12) pose an elliptic boundary value problem. We solve the problem numerically on a staggered Arakawa-C grid using finite difference method similar to that of the global tidal model implementation described by Egbert and Erofeeva (2002). The discussion of the numerical implementation is presented in this section, with details and specifics provided in Appendix B. The index notation utilized is defined in Appendix A.

4.1. Reduction to a linear system

The staggered Arakawa-C grid with schematic given in Fig. 1 is used throughout. With N denoting the number of grid-points, let $\boldsymbol{\eta},\mathbf{u},\mathbf{v}\in\mathbb{C}^N$ be complex vectors defined on the discrete η, u, and v grids of the Arakawa-C grid, respectively. The grid is staggered such that the gradient operator $\nabla\tilde{\eta}_k$ maps from the η grid to the u and v grids when discretized via backward differences. Let the finite-difference operators implementing $g\nabla\{\cdot\}$ be denoted as $\mathbf{G}_{u\leftarrow\eta},\mathbf{G}_{v\leftarrow\eta}$:

$$g\nabla\rightarrow\left\{\begin{matrix}\mathbf{G}_{u\leftarrow\eta}\\ \mathbf{G}_{v\leftarrow\eta}\end{matrix}\right\}. \tag{19}$$

In our own implementation (see Appendix B for specifics), $\mathbf{G}_{u\leftarrow\eta},\mathbf{G}_{v\leftarrow\eta}\in\mathbb{R}^{N\times N}$ are two-diagonal matrices. The subscripts $u\leftarrow\eta$ and $v\leftarrow\eta$ indicate that $\mathbf{G}_{u\leftarrow\eta}$ and $\mathbf{G}_{v\leftarrow\eta}$ provide mappings from η to u and v nodes so that vectors $(\mathbf{G}_{u\leftarrow\eta}\boldsymbol{\eta})\in\mathbb{C}^N$ and $(\mathbf{G}_{v\leftarrow\eta}\boldsymbol{\eta})\in\mathbb{C}^N$ are defined at u and v grid-points, respectively. Denote the finite-difference scheme for the matrix multiplication acting on $\nabla\tilde{\eta}_k$ in (17) as

$$\frac{1}{(\mathrm{i}\omega_k+\kappa)^2+f^2}\begin{bmatrix}\mathrm{i}\omega_k+\kappa & f\\ -f & \mathrm{i}\omega_k+\kappa\end{bmatrix}\rightarrow\left\{\begin{matrix}\mathbf{F}_{u\leftarrow u} & \mathbf{F}_{u\leftarrow v}\\ \mathbf{F}_{v\leftarrow u} & \mathbf{F}_{v\leftarrow v}\end{matrix}\right\}. \tag{20}$$

In (20), the matrices $\mathbf{F}_{u\leftarrow u},\mathbf{F}_{u\leftarrow v},\mathbf{F}_{v\leftarrow u},\mathbf{F}_{v\leftarrow v}\in\mathbb{C}^{N\times N}$ correspond to mappings between u and v grids. $\mathbf{F}_{u\leftarrow u}$ and $\mathbf{F}_{v\leftarrow v}$ map onto the same velocity grids and, therefore, are diagonal, $\mathbf{F}_{u\leftarrow v}$ and $\mathbf{F}_{v\leftarrow u}$ map across the u,v staggered grids and are four-diagonal, with the four-point stencil of u-grid-points around a v-grid-point, and vice-versa, on

an Arakawa-C grid. The velocity vectors $\mathbf{u}$ and $\mathbf{v}$ corresponding to $(\tilde{u}_k, \tilde{v}_k)$ in (16) are, thus, obtained via linear operators

$$\mathbf{U}_{u\leftarrow\eta} = -\mathbf{F}_{u\leftarrow u}\mathbf{G}_{u\leftarrow\eta} - \mathbf{F}_{u\leftarrow v}\mathbf{G}_{v\leftarrow\eta} \tag{21}$$

$$\mathbf{V}_{v\leftarrow\eta} = -\mathbf{F}_{v\leftarrow v}\mathbf{G}_{v\leftarrow\eta} - \mathbf{F}_{v\leftarrow u}\mathbf{G}_{u\leftarrow\eta} \tag{22}$$

acting on the tidal elevation vector $\boldsymbol{\eta}$

$$\begin{aligned}\mathbf{u} &= \mathbf{U}_{u\leftarrow\eta}\boldsymbol{\eta}\\ \mathbf{v} &= \mathbf{V}_{v\leftarrow\eta}\boldsymbol{\eta}.\end{aligned} \tag{23}$$

The divergence operator maps from u and v to η grid-points and is implemented via forward differences on an Arakawa-C grid

$$\mathbf{V}\cdot \rightarrow \left\{\mathbf{D}_{\eta\leftarrow u}, \mathbf{D}_{\eta\leftarrow v}\right\}, \tag{24}$$

where forward difference matrices $\mathbf{D}_{\eta\leftarrow u}, \mathbf{D}_{\eta\leftarrow v} \in \mathbb{R}^{N\times N}$ (specifics in Appendix B) are two-diagonal. With $\mathbf{H}_{u\leftarrow u}$ and $\mathbf{H}_{v\leftarrow v}$ denoting the mappings from velocities to transports (multiplication by H) at u and v grid points, the discretized second order operator (18) is expressed as

$$\mathscr{L}\{\cdot\} \rightarrow \mathbf{A}_{\eta\leftarrow\eta}, \tag{25}$$

where the matrix $\mathbf{A}_{\eta\leftarrow\eta} \in \mathbb{C}^{N\times N}$ is given by

$$\mathbf{A}_{\eta\leftarrow\eta} = \mathbf{D}_{\eta\leftarrow u}\mathbf{H}_{u\leftarrow u}\mathbf{U}_{u\leftarrow\eta} + \mathbf{D}_{\eta\leftarrow v}\mathbf{H}_{v\leftarrow v}\mathbf{V}_{v\leftarrow\eta} + \mathrm{i}\omega_k\mathbf{I}. \tag{26}$$

As described in Appendix B, the matrix $\mathbf{A}_{\eta\leftarrow\eta} \in \mathbb{C}^{N\times N}$ is nine-diagonal. Dynamics (17) is thus reduced to

$$\mathbf{A}_{\eta\leftarrow\eta}\boldsymbol{\eta} = \mathbf{0}. \tag{27}$$

The vector $\boldsymbol{\eta} \in \mathbb{C}^N$ in the foregoing contains both active, masked and boundary η-grid points. Next, we discuss the solution of (27) for the model state-space.

4.2. Solution for model state-space

Let $\mathbf{i}_{obc}$ denote the index of open boundary nodes, $\mathbf{i}_{obc} \in \mathbb{N}^{n_{obc}}$ (Appendix A). The sea surface elevation is prescribed according to (2) at $\mathbf{i}_{obc}$ grid points. We follow the index notation in Appendix A to write the discrete version of the open boundary condition (11) as

$$(\boldsymbol{\eta})_{\mathbf{i}_{obc}} = \boldsymbol{\eta}_{obc}, \tag{28}$$

where $\boldsymbol{\eta}_{obc} \in \mathbb{C}^{n_{obc}}$ are given values at open boundaries, for example prescribed from a global tidal model. Let $\mathbf{i}_{mask}$ denote the index of masked η-points, $\mathbf{i}_{mask} \in \mathbb{N}^{n_{mask}}$. The remaining η-grid points, neither in $\mathbf{i}_{mask} \in \mathbb{N}^{n_{mask}}$ nor in $\mathbf{i}_{obc}$, are the *active* nodes, with index $\mathbf{i}_{\mathbf{x}} \in \mathbb{N}^{n_{\mathbf{x}}}$, $n_{\mathbf{x}} = (N - n_{obc} - n_{mask})$. The entire vector $\boldsymbol{\eta}$ is, thus, partitioned into three subsets corresponding to active, open boundary, and masked grid points, with indices $\mathbf{i}_\eta = \{\mathbf{i}_{\mathbf{x}}, \mathbf{i}_{obc}, \mathbf{i}_{mask}\}$, where $\mathbf{i}_\eta \in \mathbb{N}^N$. The values of $\hat{\eta}_k$ at $\mathbf{i}_{\mathbf{x}}$ are the unknowns, the values at $\mathbf{i}_{obc}$ prescribe the open boundary forcing, while the values at $\mathbf{i}_{mask}$ are masked and not computed. The values $\hat{\eta}_k$ at active nodes $\mathbf{i}_{\mathbf{x}}$ are grouped into a model state-space vector $\mathbf{x} \in \mathbb{C}^{n_{\mathbf{x}}}$ defined as

$$\mathbf{x} = (\boldsymbol{\eta})_{\mathbf{i}_{\mathbf{x}}} \tag{29}$$

Let also $\mathbf{A}_{(\mathbf{x}\leftarrow\mathbf{x})}$ and $\mathbf{A}_{(\mathbf{x}\leftarrow\boldsymbol{\eta}_{obc})}$ denote the partitions of matrix $\mathbf{A}_{\eta\leftarrow\eta}$ corresponding to mappings $\mathbf{x} \leftarrow \mathbf{x}$ and $\mathbf{x} \leftarrow \boldsymbol{\eta}_{obc}$

$$\mathbf{A}_{(\mathbf{x}\leftarrow\mathbf{x})} \equiv (\mathbf{A}_{\eta\leftarrow\eta})_{\mathbf{i}_{\mathbf{x}},\mathbf{i}_{\mathbf{x}}}, \qquad \mathbf{A}_{(\mathbf{x}\leftarrow\boldsymbol{\eta}_{obc})} \equiv (\mathbf{A}_{\eta\leftarrow\eta})_{\mathbf{i}_{\mathbf{x}},\mathbf{i}_{obc}}. \tag{30}$$

Similarly, denote the partitions of matrices $\mathbf{U}_{u\leftarrow\eta}$ and $\mathbf{V}_{v\leftarrow\eta}$ in (21) and (22) corresponding to mappings $\mathbf{u} \leftarrow \mathbf{x}$ and $\mathbf{v} \leftarrow \mathbf{x}$ as

$$\mathbf{U}_{(u\leftarrow\mathbf{x})} \equiv (\mathbf{U}_{u\leftarrow\eta})_{\mathbf{i}_{\mathbf{x}},\mathbf{i}_{\mathbf{x}}}, \qquad \mathbf{V}_{(v\leftarrow\mathbf{x})} \equiv (\mathbf{V}_{v\leftarrow\eta})_{\mathbf{i}_{\mathbf{x}},\mathbf{i}_{\mathbf{x}}}. \tag{31}$$

With this notation, the linear system (27) expressed for the unknown state-space $\mathbf{x}$ is

$$\mathbf{A}_{(\mathbf{x}\leftarrow\mathbf{x})}\mathbf{x} = -\mathbf{A}_{(\mathbf{x}\leftarrow\boldsymbol{\eta}_{obc})}\boldsymbol{\eta}_{obc} \tag{32}$$

The linear system (32) is our computational discretization of the dynamical Eq. (17) at active grid-points given the open boundary conditions $\boldsymbol{\eta}_{obc}$. Note, by construction, it avoids any computations for masked grid points. The right-hand side of (32) represents ocean open boundary forcing. In our implementation, (32) is solved using a preconditioned conjugate gradient method for sparse systems (Trefethen and Bau, 1997). Since an elliptic boundary value problem (17) with BCs (11) and (12) has a unique solution, a properly formed matrix $\mathbf{A}_{(\mathbf{x}\leftarrow\mathbf{x})}$ is guaranteed to be full-rank. The rate of convergence of conjugate gradient solvers degrades as the condition number of a matrix increases. We use an incomplete LU decomposition to obtain the left and right pre-conditioners for $\mathbf{A}_{(\mathbf{x}\leftarrow\mathbf{x})}$ before applying of the conjugate gradient method.

Although the inverse matrix $\mathbf{A}^{-1}_{(\mathbf{x}\leftarrow\mathbf{x})}$ is never formed explicitly but rather the linear system $\mathbf{A}_{(\mathbf{x}\leftarrow\mathbf{x})}\mathbf{x} = \mathbf{b}$ with $\mathbf{b} = -\mathbf{A}_{(\mathbf{x}\leftarrow\boldsymbol{\eta}_{obc})}\boldsymbol{\eta}_{obc}$ is solved iteratively, we can formally write the solution of (32) and, using (23), the solution for tidal velocities $\mathbf{u}$ and $\mathbf{v}$:

$$\begin{aligned}\mathbf{x} &= \mathbf{M}_{(\mathbf{x}\leftarrow\boldsymbol{\eta}_{obc})}\boldsymbol{\eta}_{obc}\\ \mathbf{u} &= \mathbf{M}_{(\mathbf{u}\leftarrow\boldsymbol{\eta}_{obc})}\boldsymbol{\eta}_{obc}\\ \mathbf{v} &= \mathbf{M}_{(\mathbf{v}\leftarrow\boldsymbol{\eta}_{obc})}\boldsymbol{\eta}_{obc}\end{aligned} \tag{33}$$

where

$$\begin{aligned}\mathbf{M}_{(\mathbf{x}\leftarrow\boldsymbol{\eta}_{obc})} &= -\mathbf{A}^{-1}_{(\mathbf{x}\leftarrow\mathbf{x})}\mathbf{A}_{(\mathbf{x}\leftarrow\boldsymbol{\eta}_{obc})}\\ \mathbf{M}_{(\mathbf{u}\leftarrow\boldsymbol{\eta}_{obc})} &= \mathbf{U}_{(u\leftarrow\mathbf{x})}\mathbf{M}_{(\mathbf{x}\leftarrow\boldsymbol{\eta}_{obc})}\\ \mathbf{M}_{(\mathbf{v}\leftarrow\boldsymbol{\eta}_{obc})} &= \mathbf{V}_{(v\leftarrow\mathbf{x})}\mathbf{M}_{(\mathbf{x}\leftarrow\boldsymbol{\eta}_{obc})}\end{aligned} \tag{34}$$

The system (33) and (34) constitutes the discretized forward dynamical model, with forcing provided in open boundary conditions $\boldsymbol{\eta}_{obc}$.

5. Inverse estimation of open boundary conditions

5.1. Observational data and observational models

Suppose some observational data of tidal elevation and/or velocity are available in the model domain. Typically, tidal observations are collected along coasts and in inland waterways, although some measurements can come from moorings, ADCPs, and bottom mounted tide gauges. Care should be exercised in ensuring that the model resolution is sufficient to resolve the topographic features and waterways around the tide gauges utilized so that the measurements chosen for assimilation are representative of the model tidal fields. Let vectors $\boldsymbol{\eta}_{obs} \in \mathbb{C}^{n^\eta_{obs}}$, $\mathbf{u}_{obs} \in \mathbb{C}^{n^u_{obs}}$, and $\mathbf{v}_{obs} \in \mathbb{C}^{n^v_{obs}}$ contain the observed values of barotropic tidal elevations $\hat{\eta}_k$, and barotropic zonal and meridional tidal velocity components $\hat{u}_k, \hat{v}_k$ at selected observational locations. Let also $\mathbf{H}_{\boldsymbol{\eta}_{obs}\leftarrow\mathbf{x}}$, $\mathbf{H}_{\mathbf{u}_{obs}\leftarrow\mathbf{u}}$, and $\mathbf{H}_{\mathbf{v}_{obs}\leftarrow\mathbf{v}}$ denote the linear observational operators relating the state-space $\mathbf{x}$ and the gridded values of velocities $\mathbf{u}$ and $\mathbf{v}$ to the observed values $\boldsymbol{\eta}_{obs}$, $\mathbf{u}_{obs}$ and $\mathbf{v}_{obs}$, respectively. If the observations $\boldsymbol{\eta}_{obs}$, $\mathbf{u}_{obs}$ and $\mathbf{v}_{obs}$ are converted to harmonic amplitudes for barotropic tidal constituents (Appendix D) then the operators $\mathbf{H}_{\boldsymbol{\eta}_{obs}\leftarrow\mathbf{x}}$, $\mathbf{H}_{\mathbf{u}_{obs}\leftarrow\mathbf{u}}$, $\mathbf{H}_{\mathbf{v}_{obs}\leftarrow\mathbf{v}}$ merely represent the interpolation from the model grid to the observation locations. With the above notation, the data-model misfits in tidal elevation and velocity fields are given by

$$\begin{aligned}\mathbf{d}_{\boldsymbol{\eta}} &= \boldsymbol{\eta}_{obs} - \mathbf{H}_{\boldsymbol{\eta}_{obs}\leftarrow\mathbf{x}}\mathbf{x},\\ \mathbf{d}_{\mathbf{u}} &= \mathbf{u}_{obs} - \mathbf{H}_{\mathbf{u}_{obs}\leftarrow\mathbf{u}}\mathbf{u},\\ \mathbf{d}_{\mathbf{v}} &= \mathbf{v}_{obs} - \mathbf{H}_{\mathbf{v}_{obs}\leftarrow\mathbf{v}}\mathbf{v},\end{aligned} \tag{35}$$

where $(\mathbf{x}, \mathbf{u}, \mathbf{v})$ are model state-space and model velocity vectors. Lets arrange $\mathbf{d}_{\boldsymbol{\eta}}$, $\mathbf{d}_{\mathbf{u}}$, and $\mathbf{d}_{\mathbf{v}}$ into a single data-model misfit vector $\mathbf{d} \in \mathbb{C}^{n_{obs}}$ of length $n_{obs} = (n^\eta_{obs} + n^u_{obs} + n^v_{obs})$

$$\mathbf{d} = \begin{bmatrix} \mathbf{d_x} \\ \mathbf{d_u} \\ \mathbf{d_v} \end{bmatrix}_{n_{obs}} \tag{36}$$

and use $\mathbf{y} \in \mathbb{C}^{n_{obs}}$ to denote the full observational vector

$$\mathbf{y} = \begin{bmatrix} \boldsymbol{\eta}_{obs} \\ \mathbf{u}_{obs} \\ \mathbf{v}_{obs} \end{bmatrix}_{n_{obs}}. \tag{37}$$

Taking into account (23) with partitions (31), the observational operator projecting the state-space $\mathbf{x}$ onto the observational space corresponding to $\mathbf{y}$ is then given by

$$\mathbf{H} = \begin{bmatrix} \mathbf{H}_{\boldsymbol{\eta}_{obs} \leftarrow \mathbf{x}} \\ \mathbf{H}_{\mathbf{u}_{obs} \leftarrow \mathbf{u}} \mathbf{U}_{u \leftarrow \mathbf{x}} \\ \mathbf{H}_{\mathbf{v}_{obs} \leftarrow \mathbf{v}} \mathbf{V}_{v \leftarrow \mathbf{x}} \end{bmatrix}_{n_{obs} \times n_{\mathbf{x}}} \tag{38}$$

and the data-model misfits are obtained as

$$\mathbf{d} = \mathbf{y} - \mathbf{H}\mathbf{x}. \tag{39}$$

5.2. Observational and OBC error covariances

Let $\boldsymbol{\eta}$, $\mathbf{u}$, $\mathbf{v}$ denote the true values of tidal elevation and velocities on their respective staggered model grids, while $\hat{\boldsymbol{\eta}}$, $\hat{\mathbf{u}}$, $\hat{\mathbf{v}}$ denote the corresponding estimates. The true values of the gridded open boundary conditions $\boldsymbol{\eta}_{obc} \in \mathbb{C}^{n_{obc}}$ are related to the estimate $\hat{\boldsymbol{\eta}}_{obc}$ as

$$\hat{\boldsymbol{\eta}}_{obc} = \boldsymbol{\eta}_{obc} + \boldsymbol{\epsilon}_{obc} \tag{40}$$

where $\boldsymbol{\epsilon}_{obc}$ is the unknown OBC error. Let $\mathbf{B}_{obc}$ denote the open boundary condition error covariance

$$\mathbf{B}_{obc} \equiv \mathscr{E}\{\boldsymbol{\epsilon}_{obc}\boldsymbol{\epsilon}_{obc}^H\}. \tag{41}$$

In practice, $\mathbf{B}_{obc}$ is not well known (e.g., Egbert et al., 1994). It can be specified via a parametric form with some assumed OBC error parameters reflecting the accuracy information provided with the OBC values or estimated by the regional modeler. Choosing the OBC error covariance parameters amounts to specifying a statistical upper limit for the OBC correction that a modeler deems appropriate to introduce, if needed, in order to fit the dynamical model to data.

The other source of uncertainty relates to the observational error, denoted by $\boldsymbol{\epsilon}_{\mathbf{y}}$. The observational error consists of two components, the instrument error and the representativeness error (error caused by sub-scale features and by processes not represented in the model formulation). A frequent approximation is to assume that the observational error covariance matrix is diagonal

$$\mathbf{R} \equiv \mathscr{E}\{\boldsymbol{\epsilon}_{\mathbf{y}}\boldsymbol{\epsilon}_{\mathbf{y}}^H\} = \begin{bmatrix} \mathbf{R_x} & & \\ & \mathbf{R_u} & \\ & & \mathbf{R_v} \end{bmatrix}_{n_{obs} \times n_{obs}}. \tag{42}$$

This is because observations at locations sufficiently far apart are unlikely to have correlated errors of representativeness. However, any other valid covariance matrix can be specified for $\mathbf{R}$.

5.3. Inverse estimation of open boundary conditions

We seek to optimally correct an *a priori* estimate of the open boundary conditions $\hat{\boldsymbol{\eta}}_{obc}$ based on the observational data $\mathbf{y}$. Specifically, an inverse estimate

$$\hat{\boldsymbol{\eta}}_{obc}^{+} = \hat{\boldsymbol{\eta}}_{obc} + \Delta\hat{\boldsymbol{\eta}}_{obc} \tag{43}$$

is sought such that the tidal model (33) forced by $\hat{\boldsymbol{\eta}}_{obc}^{+}$

$$\begin{aligned} \mathbf{x}^{+} &= \mathbf{M}_{(\mathbf{x} \leftarrow \boldsymbol{\eta}_{obc})} \boldsymbol{\eta}_{obc}^{+} \\ \mathbf{u}^{+} &= \mathbf{M}_{(\mathbf{u} \leftarrow \boldsymbol{\eta}_{obc})} \boldsymbol{\eta}_{obc}^{+} \\ \mathbf{v}^{+} &= \mathbf{M}_{(\mathbf{v} \leftarrow \boldsymbol{\eta}_{obc})} \boldsymbol{\eta}_{obc}^{+} \end{aligned} \tag{44}$$

is optimally fitted to the data

$$\Delta\hat{\boldsymbol{\eta}}_{obc} = \arg\min J(\Delta\boldsymbol{\eta}_{obc}), \tag{45}$$

where J is the following quadratic form

$$J(\Delta\boldsymbol{\eta}_{obc}) = \Delta\hat{\boldsymbol{\eta}}_{obc}^H \mathbf{B}_{obc}^{-1} \Delta\hat{\boldsymbol{\eta}}_{obc} + (\mathbf{y} - \mathbf{H}\mathbf{x}^{+})^H \mathbf{R}^{-1} (\mathbf{y} - \mathbf{H}\mathbf{x}^{+}). \tag{46}$$

that penalizes both the data-model misfits and the values of the perturbation $\Delta\boldsymbol{\eta}_{obc}$ added to the *a priori* estimate of the open boundary conditions $\hat{\boldsymbol{\eta}}_{obc}$. The quadratic penalty (46) corresponds to the minimum error variance estimation of open boundary conditions. Note that the inverse estimate $\mathbf{x}^{+}$ in (46) is a function of OBC increment $\Delta\boldsymbol{\eta}_{obc}$ via (43) and (44). The quadratic minimization problem (45) and (46) is solved by

$$\begin{aligned} \Delta\hat{\boldsymbol{\eta}}_{obc} = {} & \mathbf{B}_{obc}\mathbf{M}_{(\mathbf{x} \leftarrow \boldsymbol{\eta}_{obc})}^H \mathbf{H}^H (\mathbf{H}\mathbf{M}_{(\mathbf{x} \leftarrow \boldsymbol{\eta}_{obc})} \mathbf{B}_{obc} \mathbf{M}_{(\mathbf{x} \leftarrow \boldsymbol{\eta}_{obc})}^H \mathbf{H}^H + \mathbf{R})^{-1} \\ & (\mathbf{y} - \mathbf{H}\mathbf{M}_{(\mathbf{x} \leftarrow \boldsymbol{\eta}_{obc})} \hat{\boldsymbol{\eta}}_{obc}) \end{aligned} \tag{47}$$

where $\hat{\boldsymbol{\eta}}_{obc}$ is the *a priori* estimate of open boundary conditions. Derivation of (47) is included as Appendix C: the term $\mathbf{B}_{obc}\mathbf{M}_{(\mathbf{x} \leftarrow \boldsymbol{\eta}_{obc})}^H \mathbf{H}^H (\mathbf{H}\mathbf{M}_{(\mathbf{x} \leftarrow \boldsymbol{\eta}_{obc})} \mathbf{B}_{obc} \mathbf{M}_{(\mathbf{x} \leftarrow \boldsymbol{\eta}_{obc})}^H \mathbf{H}^H + \mathbf{R})^{-1}$ is simply the Kalman gain for the quadratic inverse problem defined by Eqs. (43)–(46). With the OBC increment (47), the inverse open boundary condition is obtained via (43) and the dynamical Eqs. (43) and (44) are solved with the inverse OBC estimate $\hat{\boldsymbol{\eta}}_{obc}^{+}$ for $\mathbf{x}$, $\mathbf{u}$, and $\mathbf{v}$. The practical steps in computing (47) are discussed next.

5.4. Implementation of inverse OBC estimation

Firstly, we note that OBC increment $\Delta\hat{\boldsymbol{\eta}}_{obc}$ is obtained as a linear combination of error subspaces (Lermusiaux and Robinson, 1999) specified in $\mathbf{B}_{obc}$. To elucidate this point, consider the singular value decomposition of the OBC error covariance, $\mathbf{B}_{obc} = \mathbf{U}_{obc}\boldsymbol{\Lambda}_{obc}\mathbf{U}_{obc}^H$, with singular values $\boldsymbol{\Lambda}_{obc}$ (real and positive) sorted in the descending order by magnitude. Denote $\mathbf{Z}_{obc} \equiv \mathbf{U}_{obc}\boldsymbol{\Lambda}_{obc}^{1/2}$, so that

$$\mathbf{B}_{obc} = \mathbf{Z}_{obc}\mathbf{Z}_{obc}^H \tag{48}$$

Each column of matrix $\mathbf{Z}_{obc}$ specifies an orthogonal error subspace of open boundary conditions. We observe that the optimal OBC increment (47) is obtained as a linear combination of columns of $\mathbf{Z}_{obc}$

$$\Delta\boldsymbol{\eta}_{obc} = \mathbf{Z}_{obc}\mathbf{c}_{obc} \tag{49}$$

where $\mathbf{c}_{obc}$ is a vector of complex coefficients computed from data-forward model misfits. Matrix $\mathbf{Z}_{obc}$, therefore, represents a linear basis for $\Delta\boldsymbol{\eta}_{obc}$.

As discussed in Section 5.2, the specification of $\mathbf{B}_{obc}$ reflects the modeler's knowledge on the dominant parameters of the errors in the OBCs. For specific error covariances and choices of error length scales (e.g., for Gaussian-based covariances, either a Gaussian function or the second derivative of a Gaussian, (e.g., Lermusiaux et al., 2000;Lermusiaux, 2002), this model error covariance matrix has eigendecomposition properties that can be usefully employed.

With the subspaces $\mathbf{U}_{obc}$ sorted by their singular values in descending order, a position (column number) of a given subspace $(\mathbf{U}_{obc})_j$ in the matrix $\mathbf{U}_{obc}$ indicates the number of its zero-crossings in the horizontal and, therefore, a corresponding spatial length scale. For example, the subspace $(\mathbf{U}_{obc})_1$ with the largest singular value $(\boldsymbol{\Lambda}_{obc})_{1,1}$ has no zero-crossings (for most choices of Gaussian-based error covariance parameters), while the subspace $(\mathbf{U}_{obc})_{n_{obc}}$ with the smallest singular value $(\boldsymbol{\Lambda}_{obc})_{n_{obc},n_{obc}}$ has $n_{obc} - 1$ zero-crossings. The subspaces with

smaller singular values correspond to progressively smaller length scales (if this is not true due to the error parameter values chosen, the number of zero crossing is always different for each orthogonal eigenvector that are determined). Since the inverse OBC increment (49) is a linear combination of columns of $\mathbf{Z}_{obc}$, it is sensible that only the subspaces with the desired length scales are retained in $\mathbf{Z}_{obc}$

$$\mathbf{Z}_{obc,p} \equiv \mathbf{U}_{n_{obc}\times p}\ \mathbf{\Lambda}^{1/2}_{p\times p}. \tag{50}$$

The exact number p of error subspaces retained in $\mathbf{Z}_{obc}$ depends on the model domain, the regional tidal dynamics and the accuracy required by the modeler. The p subspaces (50) specify the low-rank OBC error covariance model.

The open boundary condition error subspaces propagate through the dynamical system according to

$$\begin{aligned}\mathbf{Z}_{\mathbf{x}} &= \mathbf{M}_{(\mathbf{x}\leftarrow\boldsymbol{\eta}_{obc})}\mathbf{Z}_{obc,p}\\ \mathbf{Z}_{\mathbf{u}} &= \mathbf{M}_{(\mathbf{u}\leftarrow\boldsymbol{\eta}_{obc})}\mathbf{Z}_{obc,p}\\ \mathbf{Z}_{\mathbf{v}} &= \mathbf{M}_{(\mathbf{v}\leftarrow\boldsymbol{\eta}_{obc})}\mathbf{Z}_{obc,p}\end{aligned} \tag{51}$$

The matrices $\mathbf{Z}_{\mathbf{x}}$, $\mathbf{Z}_{\mathbf{u}}$, and $\mathbf{Z}_{\mathbf{v}}$ are defined at active η, u, and v-nodes, respectively, and contain the state-space and velocity error subspaces of the forward model. We hereafter use tildes to denote a projection from the model space onto the observational space, i.e.

$$\tilde{\mathbf{Z}}_{\mathbf{x}} = \mathbf{H}_{\boldsymbol{\eta}_{obs}\leftarrow\mathbf{x}}\mathbf{Z}_{\mathbf{x}}, \qquad \tilde{\mathbf{Z}}_{\mathbf{u}} = \mathbf{H}_{\mathbf{u}_{obs}\leftarrow\mathbf{u}}\mathbf{Z}_{\mathbf{u}}, \qquad \tilde{\mathbf{Z}}_{\mathbf{v}} = \mathbf{H}_{\mathbf{v}_{obs}\leftarrow\mathbf{v}}\mathbf{Z}_{\mathbf{v}} \tag{52}$$

where $\tilde{\mathbf{Z}}_{\mathbf{x}} \in \mathbb{C}^{n^{\mathbf{x}}_{obs}\times p}$, $\tilde{\mathbf{Z}}_{\mathbf{x}} \in \mathbb{C}^{n^{\mathbf{u}}_{obs}\times p}$,, and $\tilde{\mathbf{Z}}_{\mathbf{x}} \in \mathbb{C}^{n^{\mathbf{v}}_{obs}\times p}$. With the observations given by tidal constituent harmonics (Appendix D), (52) represents an interpolation of $\mathbf{Z}_{\mathbf{x}}$, $\mathbf{Z}_{\mathbf{u}}$, and $\mathbf{Z}_{\mathbf{v}}$ to observation locations. With this notation, the data-forward model misfit covariance matrix

$$\mathbf{Q} \equiv \mathbf{H}\mathbf{M}_{(\mathbf{x}\leftarrow\boldsymbol{\eta}_{obc})}\mathbf{B}_{obc}\mathbf{M}^{H}_{(\mathbf{x}\leftarrow\boldsymbol{\eta}_{obc})}\mathbf{H}^{H} + \mathbf{R}$$

is given by

$$\mathbf{Q} = \begin{bmatrix} \tilde{\mathbf{Z}}_{\mathbf{x}}\tilde{\mathbf{Z}}^{H}_{\mathbf{x}} + \mathbf{R}_{\mathbf{x}}, & \tilde{\mathbf{Z}}_{\mathbf{x}}\tilde{\mathbf{Z}}^{H}_{\mathbf{u}}, & \tilde{\mathbf{Z}}_{\mathbf{x}}\tilde{\mathbf{Z}}^{H}_{\mathbf{v}} \\ \tilde{\mathbf{Z}}_{\mathbf{u}}\tilde{\mathbf{Z}}^{H}_{\mathbf{x}}, & \tilde{\mathbf{Z}}_{\mathbf{u}}\tilde{\mathbf{Z}}^{H}_{\mathbf{u}} + \mathbf{R}_{\mathbf{u}}, & \tilde{\mathbf{Z}}_{\mathbf{u}}\tilde{\mathbf{Z}}^{H}_{\mathbf{v}} \\ \tilde{\mathbf{Z}}_{\mathbf{v}}\tilde{\mathbf{Z}}^{H}_{\mathbf{x}}, & \tilde{\mathbf{Z}}_{\mathbf{v}}\tilde{\mathbf{Z}}^{H}_{\mathbf{u}}, & \tilde{\mathbf{Z}}_{\mathbf{v}}\tilde{\mathbf{Z}}^{H}_{\mathbf{v}} + \mathbf{R}_{\mathbf{v}} \end{bmatrix}_{n_{obs}\times n_{obs}} \tag{53}$$

The values of the coefficients $\mathbf{c}_{obc}$ in (49) are readily obtained as

$$\mathbf{c}_{obc} = [\tilde{\mathbf{Z}}^{H}_{\mathbf{x}},\ \tilde{\mathbf{Z}}^{H}_{\mathbf{u}},\ \tilde{\mathbf{Z}}^{H}_{\mathbf{v}}\ ]\mathbf{Q}^{-1}\mathbf{d} \tag{54}$$

where

$$\mathbf{d} = \mathbf{y} - \mathbf{H}\mathbf{M}_{(\mathbf{x}\leftarrow\boldsymbol{\eta}_{obc})}\hat{\boldsymbol{\eta}}_{obc} \tag{55}$$

are data-forward model misfits.

6. Methodological discussion

The proposed method seeks to control the solution of the linearized shallow water equations through the correction, $\Delta\boldsymbol{\eta}_{obc}$, added to the offshore open boundary conditions. Our present optimization of $\Delta\boldsymbol{\eta}_{obc}$ best fits the dynamical model to the observational data by keeping the magnitude and spatial structure of the OBC correction consistent with the prior OBC error covariance. Because the correction is presently introduced only through the OBCs, our inverse tidal estimate satisfies the barotropic dynamical equations exactly. More generally, additional parameters can be introduced into the control space and utilized for steering the model trajectory towards observations. For example, in certain applications the model fields are sensitive to bottom friction parameters. In this case, the procedures presented in this paper can be modified in order to add the bottom friction parameters to the control space. Theoretically, such an extension is straightforward and would require a linearization of (15) with respect to the bottom friction coefficient $\kappa(\lambda,\phi)$. The first variation of (18) with respect to κ can then be included in the right-hand-side of (32), with the rest of the methodology unchanged. In addition, an analysis increment to model bottom topography could be sought. One sensible approach is to employ a low-rank parameterization of the topographic increment and include the parameters in the control space, similarly to the OBCs. A variety of other extensions of the presented inverse method are possible and will be considered in the future.

It is useful to contrast the described method against the *representer* method which is a very useful data assimilation approach for global tidal modeling (Egbert et al., 1994; Egbert and Erofeeva, 2002). A complete and consistent overview of the *representer* method can be found in Bennett (1992, 2002). Our discussion below is only intended as a parallel to Section 5.

Given the linearized tidal dynamics (32), which we write here as

$$\mathbf{A}_{(\mathbf{x}\leftarrow\mathbf{x})}\mathbf{x} = \mathbf{f}, \tag{56}$$

with the forcing $\mathbf{f}$ provided by open boundary conditions in regional tidal applications (*viz.* Eq. (32)) or by astronomical tidal forcing in global tidal applications (Egbert and Erofeeva, 2002), combined with the observational constraint

$$\mathbf{H}\mathbf{x} = \mathbf{y}, \tag{57}$$

the *representer* method finds the generalized inverse solution

$$\mathbf{x}^{+} = \mathbf{x} + \Delta\mathbf{x} \tag{58}$$

through an increment $\Delta\mathbf{x}$ found as a linear combination of the representer vectors $\mathbf{z}_i \in \mathbb{C}^{n_{\mathbf{x}}}$

$$\begin{aligned}\mathbf{Z}_{rep} &= [\mathbf{z}_1|\mathbf{z}_2|\ldots|\mathbf{z}_{n_{obs}}]_{n_{\mathbf{x}}\times n_{obs}}\\ \Delta\mathbf{x} &= \mathbf{Z}_{rep}\mathbf{c}_{rep}.\end{aligned} \tag{59}$$

Thus, the representer matrix $\mathbf{Z}_{rep}$ specifies the linear basis for analysis increment $\Delta\mathbf{x}$. Complex coefficients $\mathbf{c}_{rep}$ are obtained from data-forward model misfits $\mathbf{d}$ as

$$\mathbf{c}_{rep} = (\tilde{\mathbf{Z}}_{rep} + \mathbf{R})^{-1}\mathbf{d} \tag{60}$$

where $\mathbf{R}$ is the observational error covariance and, similarly to (52), tilde denotes projection from the model state-space onto the observational space, $\tilde{\mathbf{Z}}_{rep} = \mathbf{H}_{rep}\mathbf{Z}_{rep}$, with the observational operator $\mathbf{H}_{rep}$ (we distinguish $\mathbf{H}_{rep}$ from $\mathbf{H}$ solely to signify optional differences in implementation and choice of the observational subset/reduced basis approach). Eqs. (59) and (60) are equivalent to expanding a portion of data-forward model misfits $\mathbf{d}$ (a part of $\mathbf{d}$ corresponding to the forward model error) in the basis of the representer functions. Eq. (59) can be contrasted against Eq. (49) of our described method. In the *representer* method, the optimization is carried out in the observational space while the present regional scheme seeks the optimization in the OBC space. Computationally, the representers are obtained in two steps (Egbert et al., 1994). Firstly, the adjoint system

$$\mathbf{A}^{H}_{(\mathbf{x}\leftarrow\mathbf{x})}\boldsymbol{\alpha}_i = \mathbf{h}_i \tag{61}$$

is solved for the adjoint variables $\boldsymbol{\alpha}_i$, $i = 1, n_{obs}$. The right-hand side of (61), $\mathbf{h}_i \in \mathbb{R}^{n_{\mathbf{x}}}$, is given by a column of $\mathbf{H}^{H}$ corresponding to observation i, $\mathbf{h}_i = (\mathbf{H}^{H})_i$. In the case of observation location coinciding with a model grid-point, $\mathbf{h}_i$ is a vector of all zeros except one entry at observation location i which is set to one. Secondly, the forward system

$$\mathbf{A}_{(\mathbf{x}\leftarrow\mathbf{x})}\mathbf{z}_i = \mathbf{B}_{\mathbf{f}}\boldsymbol{\alpha}_i \tag{62}$$

is solved for the representers $\mathbf{z}_i$. The matrix $\mathbf{B}_{\mathbf{f}} \in \mathbb{R}^{n_{\mathbf{x}}\times n_{\mathbf{x}}}$ specifies the error covariance associated with the forcing $\mathbf{f}$ of the dynamical sys-

tem (56), $\mathbf{B_f} \equiv \mathscr{E}\{\epsilon_\mathbf{f}\epsilon_\mathbf{f}^H\}$. Similarly to (48), $\mathbf{B_f}$ is not well known and needs to be specified from second principles. Note that the matrix $\mathbf{B_f}$ is of much larger dimensions than $\mathbf{B}_{obc}$: it can be challenging to compute or store $\mathbf{B_f}$ for large size problems. In order to reduce the computational cost, a recursive spatial filter can be designed and applied to $\boldsymbol{\alpha}_i$ to simulate the effect of matrix multiplication by $\mathbf{B_f}$, without forming $\mathbf{B_f}$ explicitly (Purser et al., 2003).

The model state-space error covariance $\mathbf{B_x}$ is related to $\mathbf{B_f}$ via

$$\mathbf{B_x} = \mathbf{A}^{-1}_{(\mathbf{x}\leftarrow\mathbf{x})}\mathbf{B_f}\mathbf{A}^{-H}_{(\mathbf{x}\leftarrow\mathbf{x})} \tag{63}$$

Inspection of (63) and (61) and (62) reveals that the representer matrix corresponds to

$$\mathbf{Z}_{rep} = \mathbf{B_x}\mathbf{H}^H. \tag{64}$$

In other words, by design, each representer i constitutes a covariance of the model state-space error ϵ at model grid points with the model state-space error ϵ_i at observation location i, i.e., $\mathbf{z}_i = \mathbf{B_x}\mathbf{h}_i^H = \mathscr{E}\{\epsilon\epsilon_i^H\}$.

Taking into account (60), we further observe that the generalized inverse solution (58) is equivalent to

$$\mathbf{x}^+ = \mathbf{x} + \mathbf{B_x}\mathbf{H}^H(\mathbf{H}\mathbf{B_x}\mathbf{H}^H + \mathbf{R})^{-1}\mathbf{d} \tag{65}$$

which is the minimum error variance estimate of the model state-space vector $\mathbf{x}$, given observations $\mathbf{y}$ and the state-space and observational error covariances $\mathbf{B_x}$ and $\mathbf{R}$, respectively. The representer method is an efficient specific way of computing (64) and (65).

Our approach and scheme differ from the representer approach methodologically in two ways. Firstly, an optimization is carried out in the open boundary condition space rather than in the observational space. Our strategy of using the OBCs as the control space for data assimilation reflects the specifics of regional tidal modeling. As explained in Section 1, the data-driven control of open boundary conditions is desirable and needed for regional ocean applications. Secondly, our approach does not require an adjoint model. The specifics of the implementation are such that only the forward dynamical model is needed. Variations of our approach will be presented in the conclusions.

7. Barotropic Tidal Modeling in Dabob Bay/Hood Canal, WA

The approach to barotropic tidal modeling advocated in this paper was guided and developed following the need in real-world ocean applications. In October of 2007, we utilized free-surface ocean models and acoustic models for real-time forecasting in Dabob Bay/Hood Canal region of WA within the framework of the Persistent Littoral Undersea Surveillance Network (PLUSNet) project. The modeling component of PLUSNet required that the barotropic tidal forcing for several nested domains of the primitive

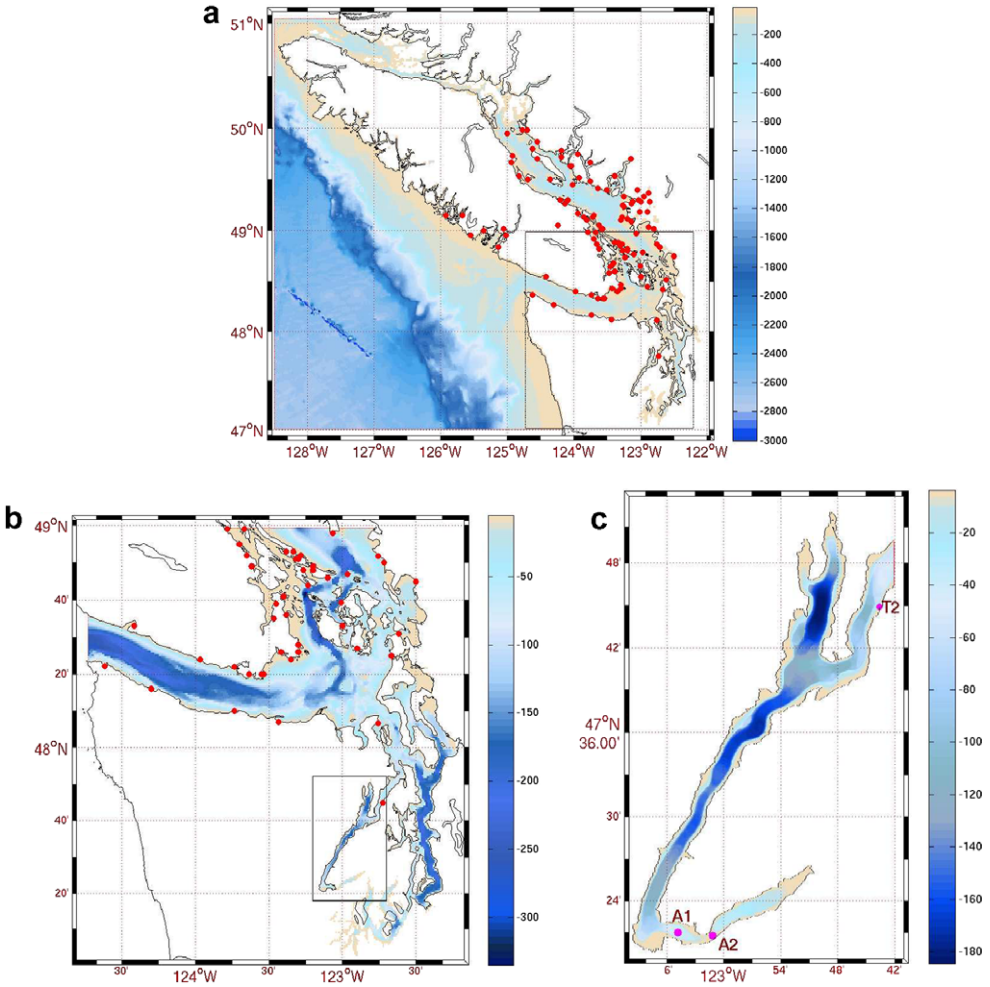

Fig. 2. Model nested domains and bottom topography [m]. Red dots show assimilated tide gauges. Validation ADCPs A1 and A2 and tide gauge T2 in Hood Canal are shown with magenta dots. (a) Outer domain around Vancouver Island. Black lines show nested Buffer domain. (b) Buffer domain covering Strait of Juan de Fuca and the enclosed islands. Black lines show nested Dabob Bay/Hood Canal domain. (c) High-resolution domain around Dabob Bay and the Hood Canal. (For interpretation of color mentioned in this figure the reader is referred to the web version of the article.)

equation model be specified. A description of the experiment is available at http://modelseas.mit.edu/Sea_exercises/PLUSNet07/. Fig. 2 shows the location and the bottom topography of Dabob Bay/Hood Canal region of WA and the surrounding basin. Dabob Bay/Hood Canal are connected to the ocean through a series of inland waterways, with complex shorelines and highly complex bottom topography. Incoming tides are funneled through a series of shallow sills and a succession of narrowing and broadening bays as they travel through the Strait of Juan de Fuca and the enclosed straits toward Dabob Bay/Hood Canal basin. Given the complexity of shoreline and bottom topography, tidal modeling in that region is particularly challenging and presents an opportunity to demonstrate our method.

For enclosed regional-scale basins, such as Dabob Bay, the tidal forcing occurs through the open boundary conditions and the contribution of the astronomical tidal forcing inside the domain is negligible. In such basins, the barotropic response of the ocean to the tidal signal in the open boundary conditions (OBCs) has to be accurately modeled. To properly propagate the information from global tidal model to local scale, three nested model domains were set up (Fig. 2). The outer large scale domain was chosen such as to have an open ocean boundary resolved in the global tidal model. We have utilized TPXO7.0 1/4-degree resolution global tidal fields (Egbert and Erofeeva, 2002) to specify open boundary conditions in the forward computation of the outer domain. The Outer domain entirely encompasses Victoria Island and resolves the straits separating Victoria Island from the mainland. Smith and Sandwell (1997) (Version 9.1) 1-min resolution bottom topography was utilized in the outer domain and the model resolution was set to match the bottom topography resolution. A Buffer domain covering Strait of Juan de Fuca and the enclosed straits was setup at 1/2-min resolution and nested in the Outer domain (Fig. 2b) and a high-resolution Dabob Bay/Hood Canal domain covering the basin of interest was setup at 1/20-minute ($\sim$ 100 m) resolution and nested in the Buffer domain (Fig. 2c). Nesting implementation was one-way: an inverse solution in a larger domain was utilized to specify open boundary conditions in a nested smaller domain, however, there was no information flow from a smaller domain to a larger domain (Logutov, submitted for publication).

Water level stations of the National Water Level Observation Network (NWLON) were utilized to constrain model sea levels to observations. The NWLON stations have tidal datums established by the National Ocean Service, following the National Geodetic Reference System. The information from coastal tide gauges in the Outer and Buffer domains was assimilated to improve the estimates of open boundary conditions using the inverse method described in this paper. Assimilated tide gauges are shown with red

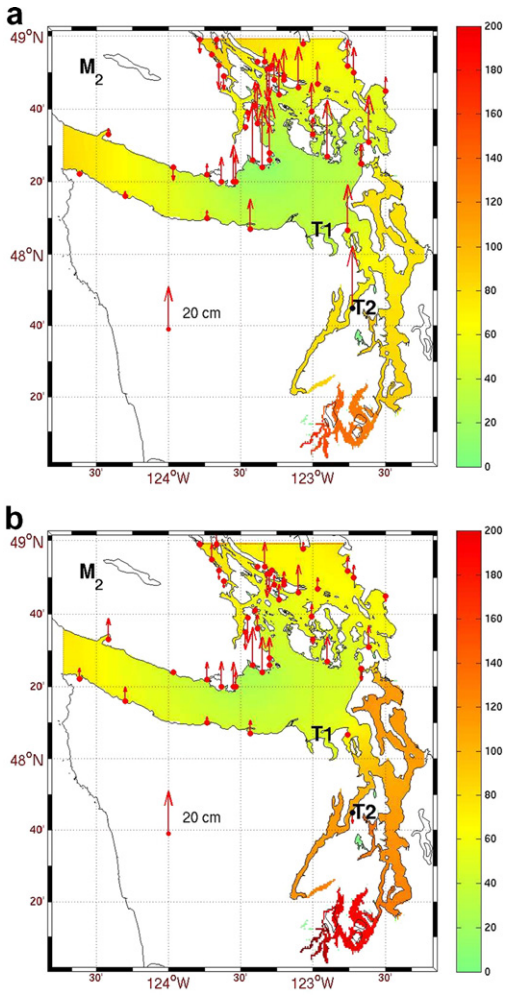

Fig. 3. M_2 sea surface height amplitude [in cm] (color) and data-model misfits (red arrows). (a) Forward solution. (b) Inverse solution. The misfits are plotted as arrows originating at observation locations and pointing up if an observed value is higher than a model value and down if otherwise. (For interpretation of color mentioned in this figure the reader is referred to the web version of the article.)

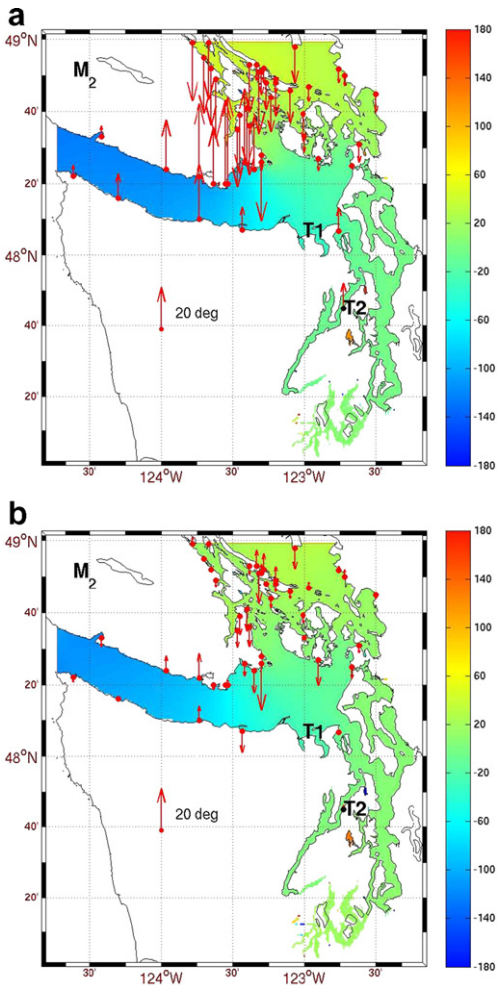

Fig. 4. M_2 co-tidal chart [Greenwich phase in deg] (color) and data-model phase misfits [in deg] (red arrows). (a) Forward solution. (b) Inverse solution. Misfits depicted as in Fig. 3. (For interpretation of color mentioned in this figure the reader is referred to the web version of the article.)

dots in Fig. 2. Computations for eight tidal constituents, M_2, K_1, O_1, S_2, P_1, and N_2 were carried out, consistently with the composition of tidal variablity observed at these water level stations. Tide gauge T2 and ADCPS A1 and A2 in Hood Canal (Fig. 2c) were allocated for validation and, therefore, not used for assimilation. Figs. 3 and 4 show the sea surface height data-model misfits (red arrows) in the Buffer domain for forward and inverse computation of M2 tidal constituent. Fig. 3 compares the amplitudes, while Fig. 4 provides the co-tidal chart and phase misfits. In general, the inverse solution can not satisfy all the observation points exactly since the utilized tidal model is limited to barotropic dynamics only and does not resolve subgrid topographical features which might influence tide gauge measurements. The inverse solution provides an optimal fit of the barotropic tidal dynamics to observational data, given assumptions made about uncertainties in the open boundary conditions and in measurements.

A Gaussian two-dimensional parametric form with length scale $L = 10$ km and variance $\sigma^2 = (15\ \text{cm})^2$ was utilized to specify the OBC error covariance in the Buffer domain. The tide gauge observational data were assumed to have uncorrelated errors, with variance $\sigma_o^2 = (1\ \text{cm})^2$, plus the representativeness error with variance $\sigma_o^2 = (4\ \text{cm})^2$. The representativeness error accounts for subgrid processes and unresolved dynamics. A slightly lower representativeness error was specified for tide gauge excepted T1 (Fig. 3) in order to steer a solution more closely to the sea-surface height observed at the main inlet leading to our main basin of interest (note resulting very small data-inverse model misfit at T1). A correction to open boundary conditions obtained from assimilation of the tide gauges and the resulting sea-surface height analysis increment are shown in Fig. 5. The increment is driven through the correction added to open boundary conditions and satisfies the barotropic tidal dynamics Eqs. (1)–(3) exactly.

The main environmental modeling focus of PLUSNet-07 experiment was Dabob Bay/Hood Canal basin (Fig. 2c). The use of the inverse methodology described in this paper has allowed us to demonstrate a very significant skill in modeling the barotropic tidal circulation in Dabob Bay/Hood Canal despite of the challenges presented by the complexity of waterways connecting this basin to the ocean. Fig. 6 shows the observed and the model sea-surface height time series for the period of PLUSNet-07 experiment. The forward solution exhibits errors of up to 30 cm (still a relatively good match given a 3.5 m range of observed total tidal elevation variations), the inverse solution is within 3 cm error bar from the observed SSH.

During the real-time phase of PLUSNet-07, no velocity measurements were available to us to validate the barotropic tidal velocity forecasts for Dabob Bay/Hood Canal region. Therefore, tidal velocity forecasts were issued and used in real-time without validation. An example of such a forecast is shown in Fig. 7. Tidal velocity forecasts were issued for every hour of the PLUSNet-07 real-time phase, a 2-week period in October of 2007. It is not until after the experiment that we had a chance to validate our forecasts by analyzing the ADCP data obtained in Hood Canal in September-October of 1994, kindly provided to us by Edward G. Josberger of the US Geological Survey. Fig. 8 shows the inverse model tidal velocities from the Dabob Bay/Hood Canal domain against the total depth averaged velocity measured by the ADCP A1 in September-October of 1994. ADCP measurements showed very little velocity variation with depth, however significant variations in the horizontal. The total flow was almost entirely driven by tides (figure not shown). The match of ADCP measurements to the velocity field which we have computed for PLUSNet-07 via the inverse method presented in this paper was impressive.

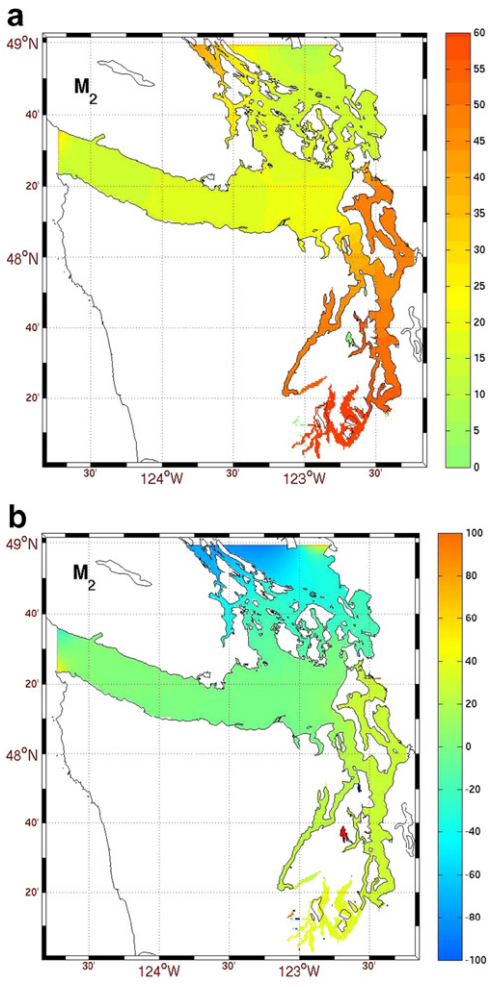

Fig. 5. Analysis increment to sea surface height in the Buffer domain for M2 tidal constituent. (a) Increment amplitude [cm]. (b) Increment phase [degrees].

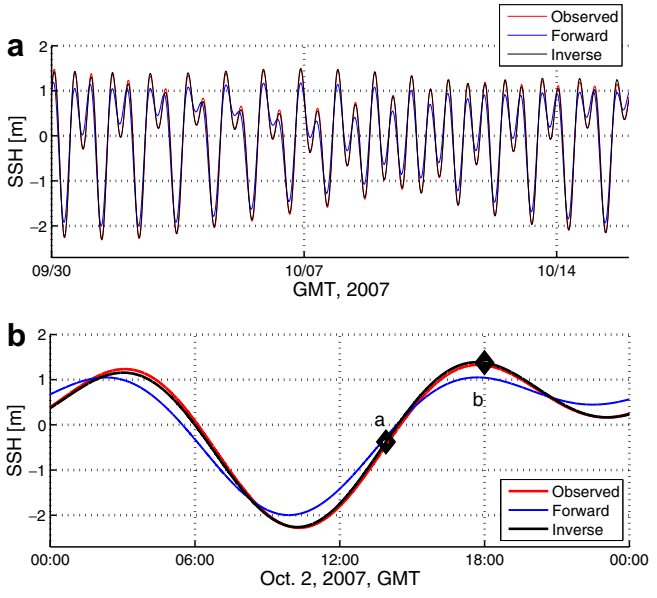

Fig. 6. Sea surface height (SSH) time series at T2 tide gauge (see location in Fig. 3). Forward and inverse model SSH presented from the computation in Dabob Bay/Hood Canal domain. (a) Entire duration of PlusNet-07 experiment. (b) October 2, 2007. Markers "a" and "b" show times of velocity field snapshots presented in Fig. 7.

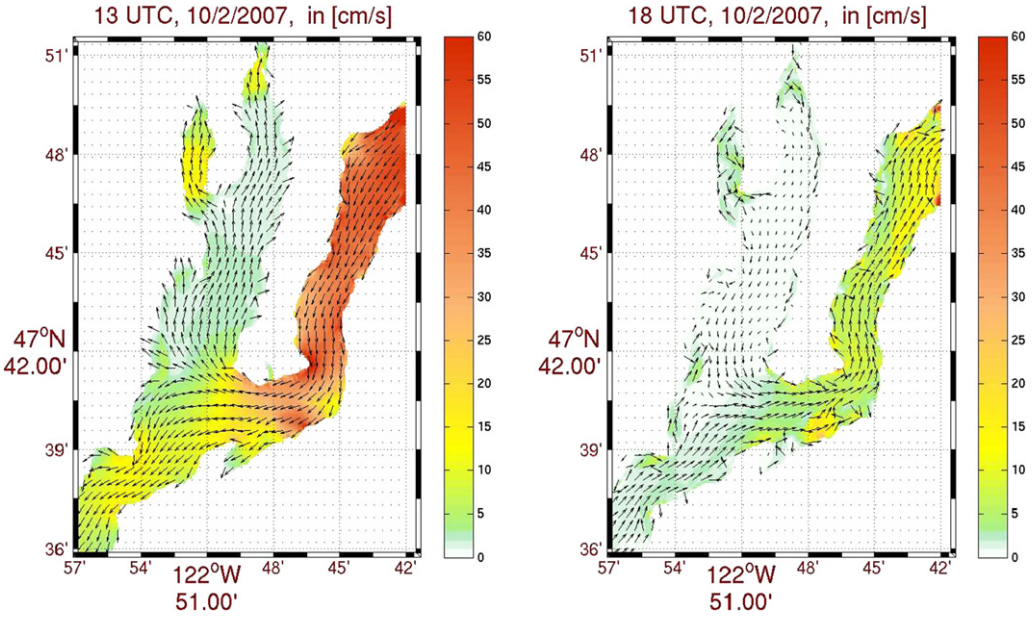

Fig. 7. Inverse estimate of tidal velocity in Dabob Bay/Hood Canal (sum of all constituents). Two snapshots corresponding to times indicated with markers "a" and "b" in Fig. 6.

To conclude, Fig. 9 compares the sea surface height analysis increment resulting from assimilation of a single tide gauge T1 using the method described in this paper and the representer method discussed in Section 6. The background error covariance $\mathbf{B}_f$ in Eq. (62) was specified as spatially uniform via a Gaussian two-dimensional parametric form with length scale $L = 10$ km and variance $\sigma_f^2 = (15\text{ cm})^2$. The difference of analysis increment from the two methods can be observed by comparing Fig. 9(a) and (b). The difference results from the underlying assumptions about sources of errors in the tidal solution. With the representer method, the inverse solution contains an additional body forcing

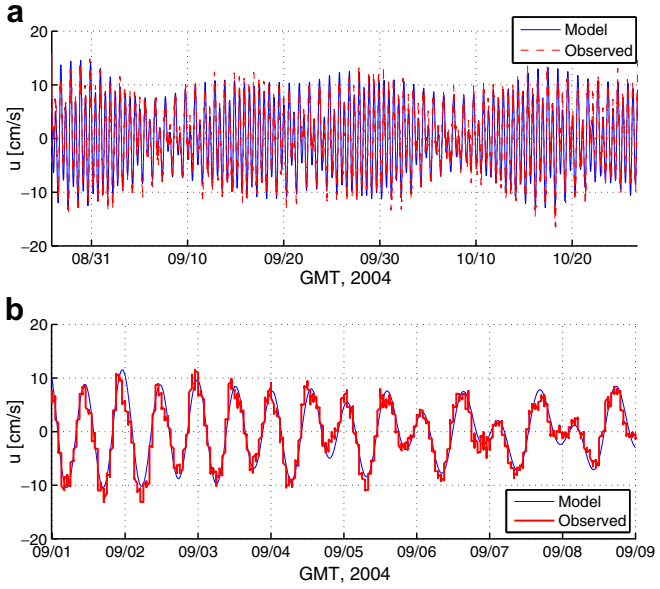

Fig. 8. Inverse model tidal velocity against observed barotropic velocity measured by ADCP A1 (see location in Fig. 2) in Dabob Bay/Hood Canal. (a) Entire period of available ADCP measurements. (b) One week period.

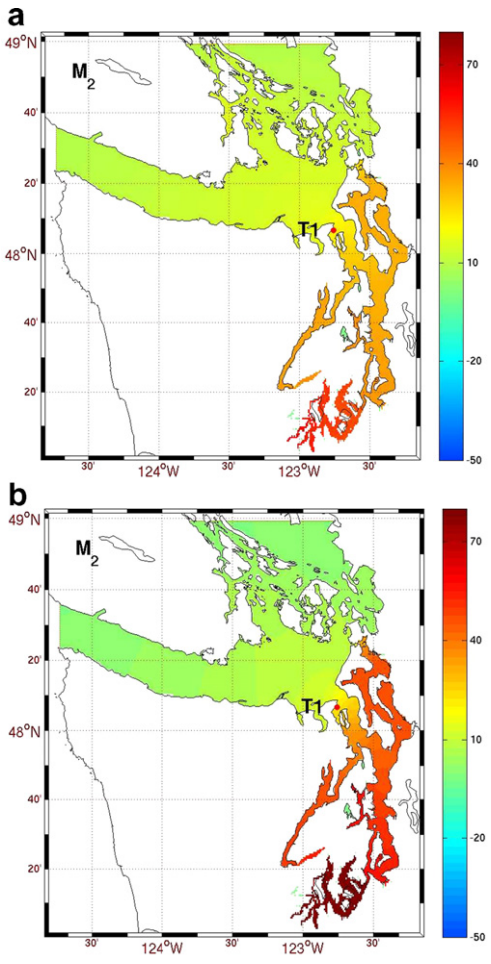

Fig. 9. Sea surface height analysis increment (real part) resulting from assimilation of tide gauge T1. (a) Computed via method described in this paper. (b) Computed via representer method.

term (Eq. (62)) that originates from an assumption about tidal model errors. With the method presented in this paper, the inverse solution is constructed following a proposition that largest errors often originate from the open boundary conditions and the inverse solution is such that it satisfies the barotropic tidal dynamics exactly. In our own practice of regional tidal modeling, the latter approach was found to be somewhat more robust and practical.

8. Conclusions

A new methodology and computational system for forward and inverse barotropic tidal modeling for regional tidal estimation have been developed. The modeling system is capable of forward (no data assimilation) tidal field predictions over high resolution bathymetry, and subsequent assimilation of tidal elevation and velocity observational data via a new practical inverse method. The forward prognostic scheme solves the linearized depth-integrated shallow water equations as a boundary value problem in the spectral domain. The inverse scheme assimilates filtered tidal velocity observations by adjusting the OBCs. After assimilation, the interior and boundary tidal fields are in accord with the tidal model and with the error covariances of the tidal observations and the prior OBC estimate. With this methodology and computational system, we have carried out accurate barotropic tidal field estimations for multi-scale nested domains including complex inland waterways is several regions of the world's oceans. To illustrate our results, such a computation was presented in the area of Dabob Bay and Hood Canal, WA.

The inverse procedures are specifically designed for regional ocean applications. We found that both high resolution and control of the barotropic model through OBCs are important elements in successful regional tidal modeling. This is because the tidal forcing is provided through the OBCs in regional ocean applications and can constitute a significant source of uncertainty. To reduce these uncertainties, the prior tidal conditions at the open boundaries need to be adjusted to the observational data, high-resolution bathymetry, and tidal dynamics. Our tidal model is fitted to data through a correction made to OBCs, consistent with the error covariances of the data and the prior OBCs. The inverse solution generated by our method presently satisfies the barotropic shallow water dynamical equations exactly.

The data assimilation scheme developed in this paper differs from previous techniques mostly by our use of a spectral-domain shallow water model and our implementation of a new inverse which is practical and does not require an adjoint model. In our method, an optimization is carried out in the OBC space rather than in the observational space or model state space as is the practice in other popular tidal data assimilation and inversion methods (e.g., representer approach, nudging, optimal interpolation, etc). Our strategy is motivated by the specifics of regional tidal modeling applications, in which the OBCs constitute a significant source of uncertainty. Our methodology and computational system are expected to continue to find wide-range applications in regional and coastal ocean science, including the estimation of barotropic tidal forcing needed for regional primitive equation modeling systems.

Variations of our approach and computational system can, of course, be further developed. For example, specific model field and parameter uncertainties can be included in the interior to account for non-linear effects and uncertainties of shallow water model parameters (e.g., bottom drag). The Error Subspace Statistical Estimation (ESSE) approach (Lermusiaux, 2002; Lermusiaux, 2006) can be additionally utilized to efficiently represent model field uncertainties at interior ocean nodes by their dominant eigenmodes. This would allow us to continue to provide timely tidal estimates in varied regions of the worlds coastal ocean. The inverse scheme could also be upgraded to include a multi-model fusion approach, with 2-D and 3-D barotropic tidal models combined together to produce the highest possible horizontal resolution, on the one hand, and resolution of the vertical velocity structure and boundary layers, on the other (Logutov, 2007). Future work could also include the implementation of our forward and inverse model on an Arakawa-B grid to add consistency with Arakawa-B formulated primitive equation models utilizing barotropic tidal forcing. Our presently linear forward modeling scheme can also be extended to a nonlinear predictor using a perturbation method and an iterative procedure, as described in Section 2. The OBCs of this nonlinear model could then be corrected at each iteration using tidal data and our inversion scheme. Finally, the fusion of the barotropic model with baroclinic tidal and internal wave models might be desirable. All together, these extensions could lead to highly accurate, data-driven barotropic and baroclinic tidal modeling at highest resolutions.

Acknowledgements

This research was supported in part by the Office of Naval Research under grants PLUSNet (S05-06), AWACS (N00014-07-1-0501) and MURI-ASAP (N00014-04-1-0534). We thank Dr. Patrick J. Haley, Jr. for useful discussions and Wayne Leslie for the management of tidal observations. We also thank the whole PLUSNet-07 (PN07) team for their collaboration and feedback before and during PN07. We are grateful to Edward G. Josberger of the US Geological Survey who has provided us with the ADCP data obtained in the Hood Canal in September-October of 1994. We would also like to thank the anonymous reviewers of this paper for their timely response and constructive suggestions and criticisms.

This is with great sadness that we learned that Prof. Peter Killworth, the founder and the Editor-in-Chief of *Ocean Modelling* from journals' inception in 1999, has passed away on the day of submition of this paper. We would like to acknowledge exceptional scientific and editorial contributions of Prof. Killworth made to the field of physical oceanography and ocean modeling and express our sincere condolences to his family and close friends.

Appendix A. Notation

$\mathbf{A} \in \mathbb{C}^{m\times n}$ complex $m \times n$ matrix,
$\mathbf{a} \in \mathbb{C}^{N}$ complex vector of length N,
$\mathbf{\Lambda}$ a diagonal matrix,
$\mathbf{A}^{H}$ transposed and complex conjugated $\mathbf{A}$,
$\mathbf{A}^{-H}$ an inverse of $\mathbf{A}^{H}$,
$(\mathbf{A})_{j}$ the (j)th column of $\mathbf{A}$,
$(\mathbf{A})_{ij}$ the (i,j)th entry of $\mathbf{A}$,
$(\mathbf{a})_{i}$ the ith entry of $\mathbf{a}$,
$\mathbb{N}$ a set of natural numbers $\{1,2,\ldots\}$,
$\mathbf{i}_K \in \mathbb{N}^K$ a set $\mathbf{i}_K = \{i_k\}_{k=1}^{K}$, $i_k \in \{1,2,\ldots\}$,
$(\mathbf{a})_{\mathbf{i}_K} \in \mathbb{C}^{K}$ comlex vector of length K containing the $\mathbf{i}_K$th entries of $\mathbf{a}$, $(\mathbf{a})_{\mathbf{i}_K} = [a_{i_1}, a_{i_2}, \ldots, a_{i_K}]^T$,
$(\mathbf{A})_{\mathbf{i}_K \mathbf{j}_L} \in \mathbb{C}^{K\times L}$ comlex $K \times L$ matrix containing the entries in the $\mathbf{i}_K$th rows and $\mathbf{j}_L$th columns of matrix $\mathbf{A}$,

$$(\mathbf{A})_{\mathbf{i}_K \mathbf{j}_L} = \begin{bmatrix} a_{i_1 j_1} & a_{i_1 j_2} & \ldots & a_{i_1 j_L} \\ a_{i_2 j_1} & a_{i_2 j_2} & \ldots & a_{i_2 j_L} \\ \vdots & \ddots & \ldots & \vdots \\ a_{i_K j_1} & a_{i_K j_2} & \ldots & a_{i_K j_L} \end{bmatrix}_{K\times L},$$

$\mathrm{vec}(\mathbf{A})$ the vector version of $\mathbf{A}$ obtained by rearranging the columns to a vector, *i.e.* $\mathrm{vec}(\mathbf{A}) = [\mathbf{a}_1^T, \mathbf{a}_2^T, \ldots, \mathbf{a}_n^T]^T$,

$\mathbf{0}_N$ the null vector of length N (all entries are zero),
$\mathbf{1}_N$ the ones vector of length N (all entries are one),
$\mathbf{A}\circ\mathbf{B}$ the Hadamard (elementwise) product of $\mathbf{A}$ and $\mathbf{B}$,
$\mathbf{A}\text{ø}\mathbf{B}$ the Hadamard (elementwise) division of $\mathbf{A}$ by $\mathbf{B}$, with special definition for zero elements in $\mathbf{B}$

$$\begin{aligned}(\mathbf{A}\text{ø}\mathbf{B})_{ij} &= (\mathbf{A})_{ij}/(\mathbf{B})_{ij} && \text{if } (\mathbf{B})_{ij}\neq 0,\\ (\mathbf{A}\text{ø}\mathbf{B})_{ij} &= 0 && \text{if } (\mathbf{B})_{ij}=0,\end{aligned} \tag{A.1}$$

$\mathbb{D}(\mathbf{a})\in\mathbb{C}^{N\times N}$ diagonal $N\times N$ matrix with vector $\mathbf{a}\in\mathbb{C}^N$ specifying the main diagonal, $(\mathbb{D}(\mathbf{a}))_{ij}=\delta_{ij}a_i$,

$\mathbb{D}_{-n}(\mathbf{a})\in\mathbb{C}^{N\times N}$ diagonal $N\times N$ matrix with vector $\mathbf{a}\in\mathbb{C}^N$ specifying the $(-n)th$ (lower) diagonal, such that $(\mathbb{D}_{-n}(\mathbf{a}))_{ij}=\delta_{i-nj}a_i$, $\mathbb{D}_{+n}(\mathbf{a})\in\mathbb{C}^{N\times N}$ diagonal $N\times N$ matrix with vector $\mathbf{a}\in\mathbb{C}^N$ specifying the $(+n)th$ (upper) diagonal, such that $(\mathbb{D}_{+n}(\mathbf{a}))_{ij}=\delta_{i+nj}a_i$, $\mathbb{D}_{+n}(\mathbf{a})=\mathbb{D}^T_{-n}(\mathbf{a})$ and $\mathbb{D}(\mathbf{a})=\mathbb{D}_{-0}(\mathbf{a})=\mathbb{D}_{+0}(\mathbf{a})$,

Appendix B. Specifics of model implementation

Below, we provide details on specification of matrices $\mathbf{G}_{u\leftarrow\eta}$, $\mathbf{G}_{v\leftarrow\eta}$, $\mathbf{F}_{u\leftarrow u}$, $\mathbf{F}_{u\leftarrow v}$, $\mathbf{F}_{v\leftarrow u}$, $\mathbf{F}_{v\leftarrow v}$, $\mathbf{D}_{\eta\leftarrow u}$, $\mathbf{D}_{\eta\leftarrow v}$, $\mathbf{H}_{u\leftarrow u}$, and $\mathbf{H}_{v\leftarrow v}$ utilized in forming the discrete model operators (21), (22), and (26).

B.1. Grids, masks, and bottom topographies

The *Arakawa-C* staggered grid, with the schematic given in Fig. 1, is utilized throughout. The coordinate of each grid point is identified in terms of latitude and longitude stored in $\mathbf{\Phi}^{grid},\mathbf{\Lambda}^{grid}\in\mathbb{R}^{m\times n}$ (lat,lon) for η,u,v-grids. Firstly, a land mask, $\mathbf{M}^\eta$, is defined at η grid points. The mask is a logical array of size $m\times n$, with entries set at ocean grid points and unset at masked/land points. The land masks for u and v grids, $\mathbf{M}^u$ and $\mathbf{M}^v$, are derived from $\mathbf{M}^\eta$ by unsetting the entries of the u,v nodes neighboring with masked η nodes, *viz* in Fig. 1, the filled symbols which indicate masked η,u,v-nodes. Let $\mathbf{m}^{grid}$ denote the vectorized model grid matrix, $\mathbf{M}^{grid}$, i.e., $\mathbf{m}^{grid}=\mathrm{vec}(\mathbf{M}^{grid})$, where $grid=\{\eta,u,v\}$.

The model does not put any restrictions on the steepness of bottom topography. However, if this inverse barotropic model is exercised in conjunction with a primitive equation model, the bottom topographies at their open boundaries should be consistent. Let $\mathbf{H}^\eta\in\mathbb{R}^{m\times n}$ denote the values of bottom topography at η-grid points, positive for ocean nodes. The bottom topography at u and v grids, $\mathbf{H}^u,\mathbf{H}^v\in\mathbb{R}^{m\times n}$ are needed in (26). On an Arakawa-C grid, this is computed from $\mathbf{H}^\eta$ following

$$\begin{aligned}H^u_{ij} &= (H^\eta_{ij}+H^\eta_{ij-1})/(M^\eta_{ij}+M^\eta_{ij-1}) && \text{if } M^u_{ij}=1\\ H^u_{ij} &= 0 && \text{if } M^u_{ij}=0\\ H^v_{ij} &= (H^\eta_{ij}+H^\eta_{i-1j})/(M^\eta_{ij}+M^\eta_{i-1j}) && \text{if } M^v_{ij}=1\\ H^v_{ij} &= 0 && \text{if } M^v_{ij}=0.\end{aligned} \tag{B.1}$$

With $\mathbf{h}^{grid}=\mathrm{vec}(\mathbf{H}^{grid})$, the operators

$$\mathbf{H}_{u\leftarrow u}=\mathbb{D}(\mathbf{h}^u),\qquad \mathbf{H}_{v\leftarrow v}=\mathbb{D}(\mathbf{h}^v) \tag{B.2}$$

define mappings from tidal velocities to transports (26) on u and v grids, respectively. Note that mappings $u\leftarrow\eta$ and $v\leftarrow\eta$ are given by backward differences and mappings $\eta\leftarrow u$ and $\eta\leftarrow v$ by forward differences on an *Arakawa-C* grid. We zero-pad the boundary elements to maintain $m\times n$ dimensionality of matrices.

B.2. Gradient and divergence operators

On a staggered *Arakawa-C* grid, the forward difference operators in the zonal x and meridional y directions

$$\begin{aligned}\mathbf{\Delta}^{frwd}_\lambda &= \mathbb{D}_{+m}(\mathbf{1}_N)-\mathbb{D}(\mathbf{1}_N)\\ \mathbf{\Delta}^{frwd}_\phi &= \mathbb{D}_{+1}(\mathbf{1}_N)-\mathbb{D}(\mathbf{1}_N)\end{aligned} \tag{B.3}$$

define the mappings from the u and v grids onto the η grid (schematic in Fig. 1), while the backward difference operators

$$\begin{aligned}\mathbf{\Delta}^{bcwd}_\lambda &= \mathbb{D}(\mathbf{1}_N)-\mathbb{D}_{-m}(\mathbf{1}_N)\\ \mathbf{\Delta}^{bcwd}_\phi &= \mathbb{D}(\mathbf{1}_N)-\mathbb{D}_{-1}(\mathbf{1}_N)\end{aligned} \tag{B.4}$$

define mappings from η-grid onto u and v grids, respectively. Thus, the gradient operator $g\mathbf{\nabla}\{\cdot\}$ in (19) which maps from η to u and v grid-points is implemented via backward differences

$$\begin{aligned}\mathbf{G}_{u\leftarrow\eta} &= \mathbb{D}(\mathbf{g}_{u\leftarrow\eta})\mathbf{\Delta}^{bcwd}_\lambda\\ \mathbf{G}_{v\leftarrow\eta} &= \mathbb{D}(\mathbf{g}_{v\leftarrow\eta})\mathbf{\Delta}^{bcwd}_\phi\end{aligned} \tag{B.5}$$

where the diagonal matrices $\mathbb{D}(\mathbf{g}_{u\leftarrow\eta})$ and $\mathbb{D}(\mathbf{g}_{v\leftarrow\eta})$ correspond to metric terms in $g\mathbf{\nabla}\{\cdot\}$ (g is acceleration due to gravity):

$$\begin{aligned}\mathbf{g}_{u\leftarrow\eta} &= g\cdot(\mathbf{1}_N\text{ø}\boldsymbol{\delta}^\lambda_{u\leftarrow\eta})\\ \mathbf{g}_{v\leftarrow\eta} &= g\cdot(\mathbf{1}_N\text{ø}\boldsymbol{\delta}^\phi_{v\leftarrow\eta}),\end{aligned} \tag{B.6}$$

where $\boldsymbol{\delta}^\lambda_{u\leftarrow\eta}$, $\boldsymbol{\delta}^\phi_{v\leftarrow\eta}$ represent metric terms on a spherical grid. Similarly, the divergence operator (24) maps from u and v to η grid-points and is implemented via forward differences

$$\begin{aligned}\mathbf{D}_{\eta\leftarrow u} &= \mathbb{D}(\mathbf{d}_{\eta\leftarrow u})\mathbf{\Delta}^{frwd}_\lambda\\ \mathbf{D}_{\eta\leftarrow v} &= \mathbb{D}(\mathbf{d}_{\eta\leftarrow v})\mathbf{\Delta}^{frwd}_\phi\end{aligned} \tag{B.7}$$

where the diagonal matrices $\mathbb{D}(\mathbf{d}_{\eta\leftarrow u})$ and $\mathbb{D}(\mathbf{d}_{\eta\leftarrow v})$ correspond to metric factors in $\mathbf{\nabla}\cdot\{\}$:

$$\begin{aligned}\mathbf{d}_{\eta\leftarrow u} &= \mathbf{m}^\eta\text{ø}\boldsymbol{\delta}^\lambda_{\eta\leftarrow u}\\ \mathbf{d}_{\eta\leftarrow v} &= \mathbf{m}^\eta\text{ø}\boldsymbol{\delta}^\phi_{\eta\leftarrow v}\end{aligned} \tag{B.8}$$

Since $\mathbf{d}_{\eta\leftarrow u}$ and $\mathbf{d}_{\eta\leftarrow v}$ contain the mask $\mathbf{m}^\eta$, the multiplications $(\mathbf{D}_{\eta\leftarrow u}\mathbf{u})$ and $(\mathbf{D}_{\eta\leftarrow v}\mathbf{v})$ produce zero values at masked η points for any values of $\mathbf{u}$ and $\mathbf{v}$, that is $(\mathbf{D}_{\eta\leftarrow u}\mathbf{u})_{\mathbf{i}^\eta_{mask}}=\mathbf{0}_{n^\eta_{mask}}$ and $(\mathbf{D}_{\eta\leftarrow v}\mathbf{v})_{\mathbf{i}^\eta_{mask}}=\mathbf{0}_{n^\eta_{mask}}$.

B.3. Rotational operators

Operators $\mathbf{F}_{u\leftarrow v}$ and $\mathbf{F}_{v\leftarrow u}$ in (20) map across the u,v staggered grids. The computations of their components are now described. First, the averaging operators are computed. On an *Arakawa-C* grid, a four-point stencil of v-points around an (i,j)th u-node leads to

$$\overline{v}^u_{ij}=\frac{(M^v_{ij-1}v_{ij-1}+M^v_{i+1j-1}v_{i+1j-1}+M^v_{i+1j}v_{i+1j}+M^v_{ij}v_{ij})}{(M^v_{ij-1}+M^v_{i+1j-1}+M^v_{i+1j}+M^v_{ij})} \tag{B.9}$$

interpolation rule from v to u grid. In the foregoing, $\overline{v}^u_{ij}$ is the value of the (i,j)th element of $\mathbf{v}$ interpolated to the (i,j)th u-grid point from its corresponding four-point v-grid stencil ($\overline{v}^u_{ij}$ set to zero if all the mask values in the denominator are zero). Similarly, a four-point stencil of u-points around an (i,j)th v-node leads to

$$\overline{u}^v_{ij}=\frac{(M^u_{i-1j}u_{i-1j}+M^u_{ij}u_{ij}+M^u_{ij+1}u_{ij+1}+M^u_{i-1j+1}u_{i-1j+1})}{(M^u_{i-1j}+M^u_{ij}+M^u_{ij+1}+M^u_{i-1j+1})} \tag{B.10}$$

interpolation rule from u to v grid (again, $\overline{u}^v_{ij}$ set to zero if all the mask values in the denominator are zero). In order to implement (B.9) and (B.10) in terms of averaging operators $\mathbf{S}_{u\leftarrow v}$ and $\mathbf{S}_{v\leftarrow u}$ acting on vectors defined on the v and u grids, respectively, we form the matrices $\mathbf{N}^u$ and $\mathbf{N}^v$ corresponding to the denominator in (B.9) and (B.10)

$$\begin{aligned}(\mathbf{N})^u_{ij} &= (\mathbf{M})^v_{ij-1}+(\mathbf{M})^v_{i+1j-1}+(\mathbf{M})^v_{i+1j}+(\mathbf{M})^v_{ij}\\ (\mathbf{N})^v_{ij} &= (\mathbf{M})^u_{i-1j}+(\mathbf{M})^u_{ij}+(\mathbf{M})^u_{ij+1}+(\mathbf{M})^u_{i-1j+1}\end{aligned} \tag{B.11}$$

and denote $\mathbf{n}^u = \mathrm{vec}(\mathbf{N}^u)$ and $\mathbf{n}^v = \mathrm{vec}(\mathbf{N}^v)$. The four-point averaging operators $\mathbf{S}_{u\leftarrow v}$ and $\mathbf{S}_{v\leftarrow u}$ in (B.9) and (B.10) are then obtained as (symbol definitions are in Appendix A)

$$\begin{aligned}
\tilde{\mathbf{S}}_{u\leftarrow v} &= \mathbb{D}_{-m}(\mathbf{m}^v) + \mathbb{D}_{-m+1}(\mathbf{m}^v) + \mathbb{D}(\mathbf{m}^v) + \mathbb{D}_{+1}(\mathbf{m}^v)\\
\tilde{\mathbf{S}}_{v\leftarrow u} &= \mathbb{D}_{-1}(\mathbf{m}^u) + \mathbb{D}(\mathbf{m}^u) + \mathbb{D}_{m-1}(\mathbf{m}^u) + \mathbb{D}_{+m}(\mathbf{m}^u)\\
\mathbf{S}_{u\leftarrow v} &= \mathbb{D}(\mathbf{1}_N \varnothing \mathbf{n}^u)\tilde{\mathbf{S}}_{u\leftarrow v}\\
\mathbf{S}_{v\leftarrow u} &= \mathbb{D}(\mathbf{1}_N \varnothing \mathbf{n}^v)\ \tilde{\mathbf{S}}_{v\leftarrow u}
\end{aligned} \tag{B.12}$$

Second, the values of the determinant (14) and other frequency elements are computed as follows. With vectors $\boldsymbol{\kappa}^{grid}, \mathbf{f}^{grid} \in \mathbb{R}^N$ containing the friction and Coriolis coefficients at model grid-points ($(.)^{grid}$ denotes specific staggered grid, either $\{\eta, u, v\}$) and ω denoting the tidal constituent frequency, this determinant (14) is,

$$\mathbf{q}^{grid} = (\mathrm{i}\omega\cdot\mathbf{1}_N + \boldsymbol{\kappa}^{grid}) \circ (\mathrm{i}\omega\cdot\mathbf{1}_N + \boldsymbol{\kappa}^{grid}) + \mathbf{f}^{grid} \circ \mathbf{f}^{grid} \tag{B.13}$$

and the vector frequency elements are

$$\begin{aligned}
\boldsymbol{\omega}^u &= \mathbf{m}^u \circ (\mathrm{i}\omega\cdot\mathbf{1}_N + \boldsymbol{\kappa}^u) \varnothing \mathbf{q}^u\\
\boldsymbol{\omega}^v &= \mathbf{m}^v \circ (\mathrm{i}\omega\cdot\mathbf{1}_N + \boldsymbol{\kappa}^v) \varnothing \mathbf{q}^v\\
\zeta^u &= \mathbf{m}^u \circ \mathbf{f}^u \varnothing \mathbf{q}^u\\
\zeta^v &= -\mathbf{m}^v \circ \mathbf{f}^v \varnothing \mathbf{q}^v
\end{aligned} \tag{B.14}$$

The operator matrices $\mathbf{F}_{u\leftarrow u}$ and $\mathbf{F}_{v\leftarrow v} \in \mathbb{R}^{N\times N}$ defining mappings $u \leftarrow u$ and $v \leftarrow v$ in (20) are then obtained from $\boldsymbol{\omega}^{grid}$ (B.14) as

$$\begin{aligned}
\mathbf{F}_{u\leftarrow u} &= \mathbb{D}(\boldsymbol{\omega}^u)\\
\mathbf{F}_{v\leftarrow v} &= \mathbb{D}(\boldsymbol{\omega}^v)
\end{aligned} \tag{B.15}$$

The operator matrices $\mathbf{F}_{u\leftarrow v}$ and $\mathbf{F}_{v\leftarrow u}$ in (20) defining mappings $u \leftarrow v$ and $v \leftarrow u$ across the staggered u and v grids are then finally obtained from ζ^{grid} (B.14) by utilizing the four-point stencil averaging operators (B.12)

$$\begin{aligned}
\mathbf{F}_{u\leftarrow v} &= \mathbb{D}(\zeta^u)\mathbf{S}_{u\leftarrow v}\\
\mathbf{F}_{v\leftarrow u} &= \mathbb{D}(\zeta^v)\mathbf{S}_{v\leftarrow u}
\end{aligned} \tag{B.16}$$

Matrices $\mathbf{F}_{u\leftarrow v}$ and $\mathbf{F}_{v\leftarrow u} \in \mathbb{R}^{N\times N}$ are four-diagonal. Note that because (B.14) contains the masks $\mathbf{m}^u$ and $\mathbf{m}^v$, the operators (B.15) and (B.16) produce zero velocity values at masked u and v points.

Appendix C. Optimal OBC increment

Here, we provide the derivation of (47). Consider the problem of finding optimal OBCs

$$\hat{\boldsymbol{\eta}}_{obc} = \arg\min_{\boldsymbol{\eta}} J(\boldsymbol{\eta}_{obc}), \tag{C.1}$$

with the penalty functional

$$J(\boldsymbol{\eta}_{obc}) = (\boldsymbol{\eta}_{obc} - \bar{\boldsymbol{\eta}}_{obc})^H \mathbf{B}_{obc}^{-1}(\boldsymbol{\eta}_{obc} - \bar{\boldsymbol{\eta}}_{obc}) + (\mathbf{y} - \mathbf{H}\mathbf{x})^H \mathbf{R}^{-1}(\mathbf{y} - \mathbf{H}\mathbf{x}). \tag{C.2}$$

where $\bar{\boldsymbol{\eta}}_{obc}$ is the *a-priori* OBC estimates, matrices $\mathbf{B}_{obc}$ and $\mathbf{R}$ are OBC and observational error covariances, and state-space $\mathbf{x}$ is given by

$$\mathbf{x} = \mathbf{M}_{(\mathbf{x}\leftarrow\boldsymbol{\eta}_{obc})}\boldsymbol{\eta}_{obc}. \tag{C.3}$$

Eqs. (C.1)–(C.3) are equivalent to (45), (46), and (44).

Theorem 1. *The minimization problem C.1, C.2, C.3 has a unique solution given by*

$$\begin{aligned}
\hat{\boldsymbol{\eta}}_{obc} =& \bar{\boldsymbol{\eta}}_{obc} + \mathbf{B}_{obc}\mathbf{M}^H_{(\mathbf{x}\leftarrow\boldsymbol{\eta}_{obc})}\mathbf{H}^H(\mathbf{H}\mathbf{M}_{(\mathbf{x}\leftarrow\boldsymbol{\eta}_{obc})}\mathbf{B}_{obc}\mathbf{M}^H_{(\mathbf{x}\leftarrow\boldsymbol{\eta}_{obc})}\mathbf{H}^H + \mathbf{R})^{-1}\\
&\times(\mathbf{y} - \mathbf{H}\mathbf{M}_{(\mathbf{x}\leftarrow\boldsymbol{\eta}_{obc})}\bar{\boldsymbol{\eta}}_{obc}).
\end{aligned} \tag{C.4}$$

Proof. Since matrices $\mathbf{B}_{obc}$ and $\mathbf{R}$ are covariances and, therefore, symmetric and positive definite, the quadratic penalty function (C.2) is convex and has a unique minimum. The minimum can be found in closed form by expressing the gradient of $J(\boldsymbol{\eta}_{obc})$ with respect to $\boldsymbol{\eta}_{obc}$

$$\begin{aligned}
\nabla J(\boldsymbol{\eta}_{obc}) = \mathbf{B}_{obc}^{-1}(\boldsymbol{\eta}_{obc} - \bar{\boldsymbol{\eta}}_{obc}) - \mathbf{M}^H_{(\mathbf{x}\leftarrow\boldsymbol{\eta}_{obc})}\mathbf{H}^H\mathbf{R}^{-1}(\mathbf{y}\\
- \mathbf{H}\mathbf{M}_{(\mathbf{x}\leftarrow\boldsymbol{\eta}_{obc})}\boldsymbol{\eta}_{obc})
\end{aligned} \tag{C.5}$$

and setting it to zero

$$\nabla J(\boldsymbol{\eta}_{obc}) = 0. \tag{C.6}$$

By solving (C.6) for $\boldsymbol{\eta}_{obc}$, we obtain

$$\begin{aligned}
\hat{\boldsymbol{\eta}}_{obc} = (\mathbf{B}_{obc}^{-1} + \mathbf{M}^H_{(\mathbf{x}\leftarrow\boldsymbol{\eta}_{obc})}\mathbf{H}^H\mathbf{R}^{-1}\mathbf{M}_{(\mathbf{x}\leftarrow\boldsymbol{\eta}_{obc})}\mathbf{H})^{-1}\mathbf{B}_{obc}^{-1}\bar{\boldsymbol{\eta}}_{obc} + (\mathbf{B}_{obc}^{-1}\\
+ \mathbf{M}^H_{(\mathbf{x}\leftarrow\boldsymbol{\eta}_{obc})}\mathbf{H}^H\mathbf{R}^{-1}\mathbf{M}_{(\mathbf{x}\leftarrow\boldsymbol{\eta}_{obc})}\mathbf{H})^{-1}\mathbf{M}^H_{(\mathbf{x}\leftarrow\boldsymbol{\eta}_{obc})}\mathbf{H}^H\mathbf{R}^{-1}\mathbf{y}
\end{aligned} \tag{C.7}$$

We next apply the Sherman-Morrison-Woodbury identity

$$(\mathbf{B}^{-1} + \mathbf{U}^H\mathbf{R}^{-1}\mathbf{V})^{-1} = \mathbf{B} - \mathbf{B}\mathbf{U}^H(\mathbf{V}\mathbf{B}\mathbf{U}^H + \mathbf{R})^{-1}\mathbf{V}\mathbf{B} \tag{C.8}$$

to the first term in (C.7) and the identity

$$(\mathbf{B}^{-1} + \mathbf{U}^H\mathbf{R}^{-1}\mathbf{V})^{-1}\mathbf{U}^H\mathbf{R}^{-1} = \mathbf{B}\mathbf{U}^H(\mathbf{V}\mathbf{B}\mathbf{U}^H + \mathbf{R})^{-1} \tag{C.9}$$

to the second term in (C.7).

Identities (C.8) and (C.9) are valid for any matrices $\mathbf{B}$, $\mathbf{R}$, $\mathbf{U}$, $\mathbf{V}$ of correct sizes. The validity of the Sherman-Morrison-Woodbury formula can be shown by multiplying $\mathbf{B}^{-1} + \mathbf{U}^H\mathbf{R}^{-1}\mathbf{V}$ with the right-hand side of (C.8) and showing that the result is identity. Eq. (C.9) is a corollary of (C.8) shown as lemma 1 below. By using the identities (C.8) and (C.9) with $\mathbf{U} = \mathbf{V} = \mathbf{M}_{(\mathbf{x}\leftarrow\boldsymbol{\eta}_{obc})}\mathbf{H}$ in (C.7), we obtain (C.4). □

Lemma 1. *(C.9) holds for any matrices* $\mathbf{B}$, $\mathbf{R}$, $\mathbf{U}$, $\mathbf{V}$ *of correct sizes.*

Proof.. Let $\mathbf{Q}$ denote

$$\mathbf{Q} \equiv \mathbf{V}\mathbf{B}\mathbf{U}^H + \mathbf{R}$$

By (C.8)

$$\begin{aligned}
(\mathbf{B}^{-1} + \mathbf{U}^H\mathbf{R}^{-1}\mathbf{V})^{-1}\mathbf{U}^H\mathbf{R}^{-1} &= \mathbf{B}\mathbf{U}^H\mathbf{R}^{-1} - \mathbf{B}\mathbf{U}^H(\mathbf{V}\mathbf{B}\mathbf{U}^H + \mathbf{R})^{-1}\mathbf{V}\mathbf{B}\mathbf{U}^H\mathbf{R}^{-1}\\
&= \mathbf{B}\mathbf{U}^H(\mathbf{Q}^{-1}\mathbf{Q}\mathbf{R}^{-1} - \mathbf{Q}^{-1}\mathbf{V}\mathbf{B}\mathbf{U}^H\mathbf{R}^{-1}\\
&= \mathbf{B}\mathbf{U}^H\mathbf{Q}^{-1}((\mathbf{V}\mathbf{B}\mathbf{U}^H + \mathbf{R})\mathbf{R}^{-1} - \mathbf{V}\mathbf{B}\mathbf{U}^H\mathbf{R}^{-1})\\
&= \mathbf{B}\mathbf{U}^H\mathbf{Q}^{-1}. \qquad \square
\end{aligned}$$

Appendix D. Conversion between time and spectral domains

D.1. Preliminaries

Tidal harmonic constants at tide gauges are typically tabulated following the standard convention as either an amplitude, $|u|_k$, and a Greenwich phase, κ_k^u, for each tidal constituent k, i.e., a tuple $(|u_k|, \kappa_k^u)$, or as a complex amplitude u_k

$$u_k = |u_k| e^{-\mathrm{i}\kappa_k^u}. \tag{D.1}$$

Variable u in the foregoing represents either an SSH (η), or a zonal (u) or meridional (v) component of tidal velocity. Note the minus sign for Greenwich phases in (D.1), $\kappa_k^u = -\angle u_k$, which is a universal convention. For a given tidal constituent k, every moment in time maps to an astronomical phase θ_k. An astronomical phase of a tidal constituent k at UTC time t_0^{UTC} can be obtained using astronomical tables or a `t_tide` toolbox implemented in matlab by Pawlowicz et al. (2002). The tidal time series is recovered from tidal harmonic constants $(|u_k|, \kappa_k^u)$ as

$$u_{tide}(t) = \sum_{k=1}^{q} |u_k| \cos(\omega_k t + \theta_k - \kappa_k^u) \tag{D.2}$$

or from complex u_k in (D.1) as

$$u_{tide}(t) = \mathbb{R}\left\{ \sum_{k=1}^{q} u_k \exp i(\omega_k t + \theta_k) \right\} \tag{D.3}$$

where θ_k is an astronomical phase at time $t = 0$. We also note that Greenwich phases κ_k^u are typically given corresponding to local time zones and care should be taken to ensure that time t and κ_k^u are consistent.

D.2. Velocity data

The time series of zonal and meridional velocity components u and v at point (x_i, y_i) are reconstructed from the spectral domain variables $\tilde{u}_k$ and $\tilde{v}_k$ following (8), which is equivalent to

$$u_{tide}(t) = \sum_{k=1}^{q} \left(\frac{\tilde{u}_k}{2} \exp \ \mathrm{i}(\omega_k t + \theta_k) + \frac{\tilde{u}_k^*}{2} \exp \mathrm{i}(\omega_k t + \theta_k) \right) \tag{D.4}$$

$$v_{tide}(t) = \sum_{k=1}^{q} \left(\frac{\tilde{v}_k}{2} \exp \ \mathrm{i}(\omega_k t + \theta_k) + \frac{\tilde{v}_k^*}{2} \exp \mathrm{i}(\omega_k t + \theta_k) \right) \tag{D.5}$$

where $\tilde{u}_k^*$ and $\tilde{v}_k^*$ denote complex conjugates of $\tilde{u}_k$ and $\tilde{v}_k$. In order to facilitate velocity data analysis, define a complex variable

$$U(t) \equiv u(t) + \mathrm{i}\ v(t) \tag{D.6}$$

with the real and imaginary parts given by the zonal and meridional velocity components. As directly seen from (D.4) and (D.5), the complex velocity $U_k(t)$ associated with each tidal constituent k is described as a sum of counter-clockwise rotating ($\tilde{a}_k$) and clockwise rotating ($\tilde{a}_{-k}$) complex exponents

$$U_k(t) \equiv u_k(t) + \mathrm{i}\ v_k(t) = \tilde{a}_k e^{\mathrm{i}(\omega_k t + \theta_k)} + \tilde{a}_{-k} e^{-\mathrm{i}(\omega_k t + \theta_k)}, \tag{D.7}$$

with the complex amplitudes $\tilde{a}_k$ and $\tilde{a}_{-k}$ given by

$$\tilde{a}_k = \frac{\tilde{u}_k + \mathrm{i}\tilde{v}_k}{2}, \qquad \tilde{a}_{-k} = \frac{\tilde{u}_k^* + \mathrm{i}\tilde{v}_k^*}{2}. \tag{D.8}$$

Eq. (D.7) describes an ellipse in a complex plane, with the counter-clockwise rotation of velocity vectors if $|\tilde{a}_k| > |\tilde{a}_{-k}|$ and clockwise rotation if $|\tilde{a}_k| < |\tilde{a}_{-k}|$. A velocity vector at any given moment of time is a superposition of two circular components, the first and the second terms on the right-hand-side of (D.7), rotating in the positive (counter-clockwise) and negative (clockwise) directions, respectively. The maximum current occurs when the circular components have the same phase, i.e., the positively and negatively rotating radial vectors point in the same direction. In this case, their velocity magnitudes are added and the current velocity is

$$M_k = |\tilde{a}_k| + |\tilde{a}_{-k}|. \tag{D.9}$$

M_k is the length of the *major* semi-axis of a velocity ellipse. The minimum current occurs when the circular components have 180° phase difference. In this case, the current velocity is

$$m_k = |\tilde{a}_k| - |\tilde{a}_{-k}|, \tag{D.10}$$

positive for the counter-clockwise and negative for clockwise velocity vector rotation. Thus, the magnitude of m_k is the length of the *minor* semi-axis of a velocity ellipse. A velocity ellipse degenerates into a line when $|\tilde{a}_k| = |\tilde{a}_{-k}|$. The oppositely rotating radial vectors representing the two terms on the right-hand-side of (D.7) meet (generate maximum current) at an angle

$$\phi_k = (\angle(\tilde{a}_{-k}) + \angle(\tilde{a}_k))/2 \tag{D.11}$$

($\angle$ denotes an argument of a complex number). Therefore, (D.11) provides an inclination of the major semi-axis, also referred to as *ellipse inclination*. The northern major semi-axis is typically utilized as the reference axis and, therefore, 180° is subtracted from ϕ_k, if $\phi_k > 180°$. The Greenwich phase is defined as an angle that the two oppositely rotating radial vectors have to traverse from their initial positions, $(\omega_k t + \theta_k) = 0$, before they meet each other, i.e., an angle between an initial position and the first encountered major semi-axis for either of the oppositely rotating radial vectors. Simple algebra reveals that this angle is given by

$$g_k = (\angle(\tilde{a}_{-k}) - \angle(\tilde{a}_k))/2. \tag{D.12}$$

Greenwich phase g_k describes a delay, $\Delta t = g_k/\omega_k$, of the maximum current relative to the zero astronomical phase times (i.e., moments of time when $(\omega_k t + \theta_k) = 0$). By solving (D.8) for u_k and v_k, we can obtain the tidal harmonics in terms of the exponent coefficients

$$u_k = \tilde{a}_k + \tilde{a}_{-k}^*, \qquad v_k = \mathrm{i}(\tilde{a}_{-k}^* - \tilde{a}_k) \tag{D.13}$$

where $\tilde{a}_{-k}^*$ is the conjugate of $\tilde{a}_{-k}$.

D.3. Harmonic analysis

Arrange observational data as a complex vector $\mathbf{z}_{obs} \in \mathbb{C}^{n_t}$

$$\mathbf{z}_{obs} = \mathbf{u}_{obs} + \mathrm{i}\mathbf{v}_{obs} \tag{D.14}$$

with $\mathbf{u}_{obs}$ and $\mathbf{v}_{obs} \in \mathbb{R}^{n_t}$ containing either the zonal and the meridional components of the observed currents or the observed sea surface height, in which case only the real part $\mathbf{u}_{obs}$ is needed. The time $\mathbf{t}^{UTC}$ of measurements $\mathbf{z}_{obs}$ referenced at t_0^{UTC} is arranged in a vector $\mathbf{t}_{obs} \in \mathbb{R}^{n_t}$, i.e.,

$$\mathbf{t}_{obs} = \mathbf{t}^{UTC} - t_0^{UTC}\mathbf{1}_{n_t}. \tag{D.15}$$

The astronomical phase θ_k corresponding to t_0^{UTC} can be obtained by using `t_tide` toolbox of Pawlowicz et al. (2002). Also, let column vector $\boldsymbol{\omega}_q \in \mathbb{R}^q, 2q < n_t$ denote tidal constituent frequencies.

We seek a least-squares fit of tidal constituents (D.4) and (D.5) to observational data $\mathbf{z}_{obs}$. Least-squares analysis can be carried by specifying the basis matrix

$$\mathbf{E}_{n_t \times 2q} \equiv [\mathbf{E}^+_{n_t \times q},\ \mathbf{E}^-_{n_t \times q}], \tag{D.16}$$

corresponding to (D.7), with

$$\mathbf{E}^+_{n_t \times q} = \exp(\mathrm{i}\ \mathbf{t}_{n_t}\boldsymbol{\omega}_q^T), \qquad \mathbf{E}^+_{n_t \times q} = \exp(-\mathrm{i}\ \mathbf{t}_{n_t}\boldsymbol{\omega}_q^T)$$

where exp denotes an entry-wise exponential (not a matrix exponential). By minimizing the squares of the misfits

$$\begin{aligned} \hat{\mathbf{a}} &= \arg\min_{\mathbf{a}} J(\mathbf{a}) \\ J(\mathbf{a}) &= (\mathbf{z}_{obs} - \mathbf{E}_{n \times 2q}\mathbf{a})^H (\mathbf{z}_{obs} - \mathbf{E}_{n \times 2q}\mathbf{a}) \end{aligned} \tag{D.17}$$

as a function of coefficients $\mathbf{a}$ (e.g., using the method of Lagrange multipliers), we obtain

$$\hat{\mathbf{a}} = (\mathbf{E}^H\mathbf{E})^{-1}\mathbf{E}^H\mathbf{z}_{obs} \tag{D.18}$$

Partition $\mathbf{a}$ into coefficients corresponding to $\mathbf{E}^+_{n_t \times q}$ and $\mathbf{E}^-_{n_t \times q}$

$$\mathbf{a} = \begin{bmatrix} \mathbf{a}^+ \\ \mathbf{a}^- \end{bmatrix}_{2q} \tag{D.19}$$

with $\mathbf{a}^+$ and $\mathbf{a}^- \in \mathbb{C}^q$. Values of coefficients $\mathbf{a}^+$ and $\mathbf{a}^-$ depend on the reference time utilized in the harmonic analysis procedures. Reference time is related to the astronomical phase θ_k via (D.7). Therefore, we can obtain the tidal constants $\tilde{\mathbf{a}}_k^+$ and $\tilde{\mathbf{a}}_k^-$ independent of the reference time in the harmonic analysis by absorbing θ_k into the constants

$$\tilde{a}_k = a_k \exp(-\mathrm{i}\theta_k), \qquad \tilde{a}_{-k} = a_{-k} \exp(\mathrm{i}\theta_k) \tag{D.20}$$

where $a_k = (\mathbf{a}^+_{obs})_k$ and $a_{-k} = (\mathbf{a}^-_{obs})_k$. With $\tilde{a}_k^+$ and $\tilde{a}_{-k}$, the values of complex amplitudes $\tilde{u}_k$ and $\tilde{v}_k$ in (8) are obtained following (D.13).

References

Andersen, O., Egbert, G., Erofeeva, S., Ray, R., 2006. Mapping nonlinear shallow-water tides: a look at the past and future. Ocean Dyn. 56, 416–429. 14.

Baines, P.G., 1982. On internal tide generation models. Deep Sea Res. A 29 (3), 307–338.

Bennett, A., McIntosh, P., 1982. Open ocean modeling as an inverse problem: Tidal theory. J. Phys. Oceanogr. 12, 1004–1018.

Bennett, A.F., 1992. Inverse Methods in Physical Oceanography. Cambridge Monographs on Mechanics and Applied Mathematics. Cambridge University Press, Cambridge.

Bennett, A.F., 2002. Inverse Modeling of the Ocean and Atmosphere. Cambridge University Press, Cambridge.

Bernard, P.E., Remacle, J.F., Legat, V., 2008. Boundary dicretization for high order discontinuous Galerkin computations of tidal flows around shallow water islands. Int. J. Numer. Methods Fluids, doi:10.1002/fld.1831.

Besiktepe, S.T., Lermusiaux, P.F.J., Robinson, A.R., 2003. Coupled physical and biochemical data driven simulations of massachusetts bay in late summer: real-time and post-cruise data assimilation. In: Gregoire, M., Brasseur, P., Lermusiaux, P. (Eds.), Special issue on The use of data assimilation in coupled hydrodynamic, ecological and bio-geo-chemical models of the oceans. Vol. 40. J. Mar. Syst. pp. 171–212.

Blain, C., Preller, R., Rivera, A., 2002. Tidal prediction using the advanced circulation model (ADCIRC) and a relocatable PC-based system. Oceanography 15 (1), 77–87.

Blayo, E., Debreu, L., 2005. Revisiting open boundary conditions from the point of view of characteristic variables. Ocean Modell. 9 (3), 231–252.

Canizares, R., Madsen, H., Jensen, H., Vested, H., 2001. Developments in operational shelf sea modelling in Danish waters. Estuar. Coast. Shelf Sci. 53, 595–605.

Chapman, D., 1985. Numerical treatment of cross-shelf open boundaries in a barotropic coastal ocean model. J. Phys. Oceanogr. 15, 1060–1075.

Chen, C., Beardsley, R., 1998. Tidal mixing and cross-frontal particle exchange over a finite amplitude asymmetric bank: a model study with application to Georges Bank. J. Mar. Res. 56, 1163–1201.

Das, S.K., Lardner, R.W., 1992. Variational parameter estimation for a two-dimensional numerical tidal model. Int. J. Numer. Methods Fluids 15, 313–327.

Davies, A.M., 1993. A bottom boundary layer-resolving three-dimensional tidal model: a sensitivity study of eddy viscosity formulation. J. Phys. Oceanogr. 23, 1437–1453.

Davies, A.M., Gerritsen, H., 1994. An intercomparison of three dimensional tidal hydrodynamic models of the Irish sea. Tellus 46A, 200–221.

Davies, A.M., Jones, J.E., Xing, J., 1997a. Review of recent developments in tidal hydrodynamic modelling I. Spectral models. J. Hydrol. Eng. ASCE 123, 278–292.

Davies, A.M., Jones, J.E., Xing, J., 1997b. Review of recent developments in tidal hydrodynamic modelling II: turbulence energy models. J. Hydrol. Eng. ASCE 123, 293–302.

Davies, A.M., Kwong, S.C.M., Flather, R.A., 1997c. A three dimensional model of diurnal and semi-diurnal tides on the European shelf. J. Geophys. Res. 102, 8625–8656.

Davies, H.C., 1976. A lateral boundary formulation for multi-level prediction models. Quart. J. R. Met. Soc. 102, 405–418.

Dee, D.P., 1995. On-line estimation of error covariance parameters for atmospheric data assimilation. Monthly Weather Rev. 123, 1128–1145.

Egbert, G., Bennett, A., Foreman, M. 1994. TOPEX/Poseidon tides estimated using a global inverse model. J. Geophys. Res. 99, C12, 24, 821, 24,852.

Egbert, G., Erofeeva, S., 2002. Efficient inverse modeling of barotropic ocean tides. J Atmos. Ocean. Technol. 19, 183–204.

Egbert, G.D., 1997. Tidal data inversion: interpolation and inference. Progr. Oceanogr. 40, 53–80.

Evangelinos, C., Lermusiaux, P.F.J., Geiger, S.K., Chang, R.C., Patrikalakis, N.M., 2006. Web-enabled configuration and control of legacy codes: an application to ocean modelling. Ocean Modell. 13, 197–220.

Flather, B., 1976. A tidal model of the northwest European continental shelf. Mem. Soc. R. Sci. Liege 10, 141–164.

Foreman, M.G.G., Thomson, R.E., 1997. Three dimensional model simulations of tides and buoyancy currents along the west coast of Vancouver island. J. Phys. Oceanogr. 27, 1300–1325.

Franks, P., Chen, C., 1996. Plankton production in tidal fronts: a model of Georges Bank.

Garrett, C., Gerkema, T., 2007. On the body-force term in internal-tide generation. J. Phys. Oceanogr. 37, 2172–2175.

George, K., 2007. A depth-averaged tidal numerical model using non-orthogonal curvilinear co-ordinates. Ocean Dyn. 57, 363–374.

Greenberg, D.A., Shore, J.A., Page, F.H., M., D., 2005. A finite element circulation model for embayments with drying intertidal areas and its application to the quoddy region of the bay of fundy. Ocean Modell. 10, 211–231.

Grenier, R.R., Luettich, R.A., Westerin, J.J., 1995. A comparison of non-linear frictional characteristics of two-dimensional and three-dimensional models of a shallow tidal embayment. J. Geophys. Res. 100, 13719–13735.

Haley, Jr., P.J., Lermusiaux, P.F.J., Robinson, A.R., Leslie, W.G., Logutov, O., Cossarini, G., Liang, X.S., Moreno, P., Ramp, S.R., Doyle, J., Bellingham, J., Chavez, F., Johnston, S., in press. Forecasting and reanalysis in the Monterey Bay/California current region for the Autonomous Ocean Sampling Network-II Experiment. Deep Sea Res., Part II.

He, R., Wilkin, J.L., 2006. Barotropic tides on the southeast new england shelf: a view from a hybrid data assimilative modeling approach. J. Geophys. Res. 111, C08002.

Hea, Y., Lub, X., Qiua, Z., Zhaoc, J., 2004. Shallow water tidal constituents in the Bohai Sea and the Yellow Sea from a numerical adjoint model with TOPEX/POSEIDON altimeter data. Cont. Shelf Res. 24, 1521–1529.

Heemink, A., Kloosterhuis, H., 1990. Data assimilation for non-linear tidal models. Int. J. Numer. Methods Fluids 11 (12), 1097–1112.

Hubbert, G.D., Preller, R., P.G. Posey, G., Carroll, S., 2001. Software requirements specification for the globally relocatable navy tide/atmosphere modeling system (PCTides). Memorandum Report NRL/MR/7322-01-8266, Naval Research Laboratory, Stennis Space.

Jones, J.E., Davies, A.M., 1996. A high resolution three dimensional model of theM2, M4, M6, S2, N2, K1 and O1 tides in the eastern Irish Sea. Estuar. Coast. Shelf Sci. 42, 311–346.

Kurapov, A., Egbert, G., Allen, J., Miller, R., Erofeeva, S., Kosro, P., 2003. M2 internal tide off Oregon: inferences from data assimilation. J. Phys. Oceanogr. 33, 1733–1757.

Kurapov, A.L., Egbert, G.D., Allen, J.S., Miller, R.N., 2007. Representer-based variational data assimilation in a nonlinear model of nearshore circulation. J. Geophys. Res. 112, C11019.

Lavelle, J., Thacker, W., 2008. A pretty good sponge: dealing with open boundaries in limited-area ocean models. Ocean Modell. 20, 270–292.

Le Cann, B., 1990. Barotropic tidal dynamics of the bay of biscay shelf. Cont. Shelf Res. 10 (8), 723–758.

Lee, J., Jung, K., 1999. Application of eddy viscosity closure models for the M2 tide and tidal currents in the Yellow sea and the East China sea. Cont. Shelf Res. 19 (4), 445–475.

LeProvost, C., Genco, M.L., Lyard, F., Vincent, P., Canceil, P., 1994. Spectroscopy of the world ocean tides from a finite element hydrodynamic model. J. Geophys. Res. 99(C12), 24777–24798.

LeProvost, C., Rougier, G., Poncet, A., 1981. Numerical modeling of the harmonic constituents of the tides, with application to the English channel. J. Phys. Oceanogr. 11, 1123–1138.

LeProvost, C., Vincent, P., 1986. Some tests of precision for a finite element model of ocean tides. J. Comput. Phys. 65, 273–291.

Lermusiaux, P.F.J., 1997. Error subspace data assimilation methods for ocean field estimation: theory, validation and applications (Harvard Ocean Prediction System). Ph.D. thesis, Harvard University.

Lermusiaux, P.F.J., 1999. Data assimilation via error subspace statistical estimation. part II: Mid-atlantic bight shelfbreak front simulations, and esse validation. Monthly Weather Rev. 127 (8), 1408–1432.

Lermusiaux, P.F.J., 2002. On the mapping of multivariate geophysical fields: sensitivity to size, scales and dynamics. J. Atmos. Ocean. Technol. 19, 1602–1637.

Lermusiaux, P.F.J., 2006. Uncertainty estimation and prediction for interdisciplinary ocean dynamics. J. Comput. Phys. 217, 176–199.

Lermusiaux, P.F.J., 2007. Adaptive modeling, adaptive data assimilation and adaptive sampling. Physica D 230, 172–196.

Lermusiaux, P.F.J., Anderson, D.G., Lozano, C.J., 2000. On the mapping of multivariate geophysical fields: error and variability subspace estimates. Quart. J. R. Met. Soc., 1387–1430.

Lermusiaux, P.F.J., Chiu, C.-S., 2002. Four-dimensional data assimilation for coupled physical-acoustical fields. In: Pace, N., Jensen, F. (Eds.), Acoustic Variability. Kluwer, Academic Press, pp. 417–424.

Lermusiaux, P.F.J., Chiu, C.S., Gawarkiewicz, G.G., Abbot, P., Robinson, A.R., Miller, R., Haley, P., Leslie, W., Majumdar, S., Pang, A., Lekien, F., 2006. Quantifying uncertainities in ocean predictions. Oceanography 19 (1), 92–105.

Lermusiaux, P.F.J., Evangelinos, C., Tian, R., Haley, P., McCarthy, J., Patrikalakis, N., Robinson, A., Schmidt, H., 2004. Adaptive coupled physical and biogeochemical ocean predictions: a conceptual basis. In: Lecture Notes in Computer Science. Vol. 3038 of Computational Science – ICCS 2004. Springer, Germany, pp. 685–692.

Lermusiaux, P.F.J., Robinson, A.R., 1999. Data assimilation via error subspace statistical estimation. part I: theory and schemes. Monthly Weather Rev. 127 (7), 1385–1407.

Logutov, O.G., 2007. Multi-model fusion and uncertainty estimation for ocean prediction. Ph.D. thesis, Harvard University.

Logutov, O.G., submitted for publication. A multi-grid methodology for assimilation of measurements into regional tidal models. Ocean Dynamics.

Logutov, O.G., Robinson, A.R., 2005. Multi-model fusion and error parameter estimation. Quart. J. R. Met. Soc. 131, 3397–3408.

Luettich, R., Westerink, J.J., Scheffner, N., 1992. ADCIRC: an advanced three-dimensional circulation model for shelves coasts and estuaries, report 1: theory and methodology of ADCIRC-2DDI and ADCIRC-3DL. Dredging Research Program Technical Report DRP-92-6, U.S. Army Engineers Waterways Experiment Station, Vicksburg, MS, 137 p.

Lynch, D., Naimie, C.E., 1993. The M2 tide and its residual on outer banks of the Gulf of Maine. J. Phys. Oceanogr. 23, 2222–2253.

Lynch, D.R., Gray, W.G., 1979. A wave equation model for finite element tidal computations. Comput. Fluids 7, 207–228.

Marchesiello, P., McWilliams, J., Shchepetkin, A., 2001. Open boundary condition for long-term integration of regional oceanic models. Ocean Modell. 3, 1–20.

McIntosh, P., Bennett, A.F., 1984. Open ocean modeling as an inverse problem: M2 tides in Bass strait. J. Phys. Oceanogr. 14, 601–614.

McLaughlin, J., Bilgili, A., Lynch, D., 2003. Numerical modeling of tides in the Great Bay estuarine system: dynamical balance and spring-neap residual modulation. Estuar. Coast. Shelf Sci. 57, 283–296.

Moody, J.A., Butman, B., Beardsley, R.C., Brown, W.S., Daifuku, P., Irish, J.D., Mayer, D.A., Mofjeld, H.O., Petrie, B., Ramp, S., Smith, P., Wright, W.R., 1984. Atlas of tidal elevation and current observations on the Northeast American continental shelf and slope. U.S. Geol. Surv., 122 pages. U.S. Geological Survey Bulletin, U.S. Government Printing Office.

Oddo, P., Pinardi, N., 2008. Lateral open boundary conditions for nested limited area models: a scale selective approach. Ocean Modell. 20, 134–156.

Orlanski, I., 1976. A simple boundary condition for unbounded hyperbolic flows. J. Comput. Phys. 21, 251–269.

Parker, B.B., 1991. The Relative Importance of the Various Nonlinear Mechanisms in a Wide Range of Tidal Interaction (review). Tidal Hydrodynamics. John Wiley and Sons. pp. 237–268.

Pawlowicz, B., Beardsley, B., Lentz, S., 2002. Classical tidal harmonic analysis including error estimates in MATLAB using T TIDE. Comput. Geosci. 28, 929–937.

Purser, R.J., Wu, W.-S., Parrish, D.F., Roberts, N.M., 2003. Numerical aspects of the application of recursive filters to variational statistical analysis. Part i: Spatially homogeneous and isotropic gaussian covariances. Monthly Weather Rev. 131, 1524–1535.

Robinson, A., 1999. Forecasting and simulating coastal ocean processes and variabilities with the Harvard Ocean Prediction System. In: Mooers, C. (Ed.), Coastal Ocean Prediction. AGU Coastal and Estuarine Studies Series. American Geophysical Union, pp. 77–100.

Robinson, A.R., Lermusiaux, P.F.J., Sloan, N., 1998. Data assimilation. In: Brink, K., Robinson, A. (Eds.), Processes and Methods. Vol. 10 of The Sea: The Global Coastal Ocean. John Wiley and Sons, New York, pp. 541–594.

Shulman, I., Wu, C.-R., Lewis, J., Paduan, J., Rosenfeld, L., Kindle, J., Ramp, S.R., Collins, C., 2002. High resolution modeling and data assimilation in the Monterey Bay area. Cont. Shelf Res. 22, 1129–1151.

Shum, C.K., Woodworth, P., Anderson, O., Egbert, G., Francis, O., King, C., Klosko, S., LeProvost, C., Li, X., Molines, J.-M., Parke, M., Ray, R., Schlax, M., Stammer, D., Tierney, C., Vincent, P., Wunsch, C., 1997. Accuracy assessment of recent ocean tide models. J. Geophys. Res. 102 (C11). 25,173– 25,194.

Simpson, J., 1998. Tidal processes in shelf seas. Vol. 10 of The Sea: The Global Coastal Ocean. John Wiley and Sons, New York.

Smith, W.H.F., Sandwell, D.T., 1997. Global seafloor topography from satellite altimetry and ship depth soundings. Science 277, 1957–1962.

Snyder, R., Sidjabat, M., Filloux, J., 1979. A study of tides, setup and bottom friction in a shallow semi-enclosed basin. part II: Tidal model and comparison with data. J. Phys. Oceanogr. 9, 170–188.

Sorensen, J.V., Madsen, H., 2004. Efficient Kalman filter techniques for the assimilation of tide gauge data in three-dimensional modeling of the North Sea and Baltic Sea system. J. Geophys. Res. 109 (C03017), 1–14.

Trefethen, L., Bau, D., 1997. Numerical Linear Algebra. SIAM Publications, New York.

Tsynkov, S., 1998. Numerical solution of problems on unbounded domains. A review. Appl. Numer. Math. 27, 465–532.

Xing, J., Davies, A.M., 1996. Application of turbulence energy models to the computation of tidal currents and mixing intensities in shelf edge regions. J. Phys. Oceanogr. 26, 417–447.

Xu, J., Lermusiaux, P.F.J., Haley, P.J., Leslie, W.G., Logutov, O.G., 2008. Spatial and temporal variations in acoustic propagation in Dabob Bay during PLUSNet-07 exercise. In: 'Underwater Acoustics' Conference Proceedings. Acoustics'08 ASA/EAA. Paris.

Zou, J., Hsieh, W.H., Navon, I.M., 1995. Sequential open-boundary control by data assimilation in a limited-area model. Monthly Weather Rev. 123, 2899–2909.